The yeast dynein Dyn2-Pac11 complex is a dynein dimerization/processivity factor: structural and single-molecule characterization

Lu Rao[a,*], Erin M. Romes[b,c,*], Matthew P. Nicholas[a,d], Sibylle Brenner[a], Ashutosh Tripathy[b], Arne Gennerich[a,†], and Kevin C. Slep[e,†]

[a]Department of Anatomy and Structural Biology and Gruss Lipper Biophotonics Center and [d]Medical Scientist Training Program, Albert Einstein College of Medicine, New York, NY 10461; [b]Department of Biochemistry and Biophysics, [c]Graduate Program in Molecular Biophysics and Biochemistry, and [e]Department of Biology, University of North Carolina at Chapel Hill, Chapel Hill, NC 27599

ABSTRACT **Cytoplasmic dynein is the major microtubule minus end–directed motor. Although studies have probed the mechanism of the C-terminal motor domain, if and how dynein's N-terminal tail and the accessory chains it binds regulate motor activity remain to be determined. Here, we investigate the structure and function of the *Saccharomyces cerevisiae* dynein light (Dyn2) and intermediate (Pac11) chains in dynein heavy chain (Dyn1) movement. We present the crystal structure of a Dyn2-Pac11 complex, showing Dyn2-mediated Pac11 dimerization. To determine the molecular effects of Dyn2 and Pac11 on Dyn1 function, we generated *dyn2*Δ and *dyn2*Δ*pac11*Δ strains and analyzed Dyn1 single-molecule motor activity. We find that the Dyn2-Pac11 complex promotes Dyn1 homodimerization and potentiates processivity. The absence of Dyn2 and Pac11 yields motors with decreased velocity, dramatically reduced processivity, increased monomerization, aggregation, and immobility as determined by single-molecule measurements. Deleting *dyn2* significantly reduces Pac11-Dyn1 complex formation, yielding Dyn1 motors with activity similar to Dyn1 from the *dyn2*Δ*pac11*Δ strain. Of interest, motor phenotypes resulting from Dyn2-Pac11 complex depletion bear similarity to a point mutation in the mammalian dynein N-terminal tail (*Loa*), highlighting this region as a conserved, regulatory motor element.**

Monitoring Editor
Xueliang Zhu
Chinese Academy of Sciences

Received: Mar 28, 2013
Revised: Jun 3, 2013
Accepted: Jun 6, 2013

INTRODUCTION

Cytoplasmic dynein is a microtubule (MT) minus end–directed motor complex involved in mitotic spindle formation and positioning, as well as in removing kinetochore-bound anaphase-wait checkpoint components (Pfarr *et al.*, 1990; Steuer *et al.*, 1990; Bader and Vaughan, 2010). In interphase, cytoplasmic dynein organizes the MT array and transports cargoes, including organelles and vesicles from peripheral regions to the cell center (Vale, 2003). When anchored at the cell cortex or at kinetochores, dynein captures MTs and pulls them toward its anchor site (Adames and Cooper, 2000; Tulu *et al.*, 2006). In cilia, cytoplasmic dynein (cytoplasmic dynein 2) facilitates retrograde intraflagellar transport from the tip of the cilium back toward the cell body (Signor *et al.*, 1999). Collectively, cytoplasmic dynein is the major MT minus end–directed processive motor in eukaryotic cells. However, the structural determinants that allow the native motor to dimerize and move processively remain to be determined.

The dynein heavy chain (HC) is composed of an N-terminal dimerization/cargo-binding domain and a C-terminal motor domain. The motor domain comprises a hexameric array of AAA+ ATPase domains (AAA+: ATPase associated with various cellular activities), a subset of which hydrolyze ATP to drive conformational changes of the force- and displacement-generating linker element and the

This article was published online ahead of print in MBoC in Press (http://www.molbiolcell.org/cgi/doi/10.1091/mbc.E13-03-0166) on June 12, 2013.

*These authors contributed equally; †These authors contributed equally.

Address correspondence to: Arne Gennerich (arne.gennerich@einstein.yu.edu), Kevin C. Slep (kslep@bio.unc.edu).

Abbreviations used: DMB, dynein motility buffer; EMCCD, electron-multiplying charge-coupled device; HC, heavy chain; IC, intermediate chain; ITC, isothermal titration calorimetry; LC, light chain; LIC, light intermediate chain; Loa, legs at odd angles; MT, microtubule; NHS, *N*-hydroxysuccinimide; QT, glutamine-threonine; rmsd, root-mean-square deviation; SEC-MALS, size exclusion chromatography and multiangle light scattering; TIRF, total internal reflection fluorescence; TMR, tetramethylrhodamine; WT, wild type.

Supplemental Material can be found at:
http://www.molbiolcell.org/content/suppl/2013/06/10/mbc.E13-03-0166v1.DC1.html

MT-binding stalk (Burgess *et al.*, 2003; Carter *et al.*, 2008, 2011), effectively coordinating phases of ATP hydrolysis and nucleotide exchange with MT binding, motor domain motions, and MT release (Kon *et al.*, 2004, 2005; Reck-Peterson *et al.*, 2006; Imamula *et al.*, 2007). Although recent electron microscopy (Burgess *et al.*, 2003; Roberts *et al.*, 2009) and crystallographic studies (Kon *et al.*, 2012; Schmidt *et al.*, 2012) illuminate ATP-dependent structural changes underlying the dynein motility mechanism, little is known about the factors that bind the dynein N-terminal region and their potential to regulate dynein motor activity.

In contrast to the expansive MT plus end–directed kinesin motor family, eukaryotes contain a single cytoplasmic dynein heavy chain gene (excluding many plant species that lack cytoplasmic dynein altogether). To perform specific biological functions, the cytoplasmic dynein heavy chain engages a subset of diverse proteins that facilitate differential cargo attachment and motor regulation. The dynein heavy chain N-terminal domain binds a number of accessory proteins directly, including the dynein intermediate chain (IC) and light-intermediate chain (LIC; Tynan *et al.*, 2000). Human cytoplasmic dynein is essential to cellular function and performs diverse tasks by differentially recruiting a subset of accessory factors from a pool of 19 known proteins (Wickstead and Gull, 2007). In contrast, the *Saccharomyces cerevisiae* dynein heavy chain (Dyn1) is not essential and is exclusively used to position the mitotic spindle (Eshel *et al.*, 1993; Li *et al.*, 1993). *dyn1*Δ cells are viable due to Cin8 activity, which redundantly positions the mitotic spindle, although *dyn1*Δ cells exhibit spindle-positioning defects, delayed mitosis, and an increased percentage of binucleate mother cells (Eshel *et al.*, 1993; Saunders *et al.*, 1995; Geiser *et al.*, 1997). Restricted to this single function, yeast Dyn1 has a limited number of subunits and accessory proteins, which include the IC (Pac11), LIC (Dyn3), light chain (LC; Dyn2), Lis1 (Pac1), Nudel (Ndl1), and the dynactin complex (Lee *et al.*, 2003; Li *et al.*, 2005; Wickstead and Gull, 2007; Stuchell-Brereton *et al.*, 2011).

Dynein ICs are composed of a predicted N-terminal coiled coil, followed by LC binding sites and a C-terminal WD-40 repeat/β-propeller domain (Figure 1A). The metazoan IC N-terminal region interacts with the $p150^{Glued}$ subunit of the dynactin complex (Nip100 in yeast; Moore *et al.*, 2008), a key regulator of dynein motor activity (Karki and Holzbaur, 1995; King *et al.*, 2003; Ross *et al.*, 2006; Kardon *et al.*, 2009). Metazoan ICs bind three distinct dynein LCs: TcTex, LC8, and LC7 (Mok *et al.*, 2001; Makokha *et al.*, 2002; Susalka *et al.*, 2002). These three dynein LCs bind distinct motifs that bridge the IC's N-terminal coiled coil and the C-terminal WD-40 repeat domain. Each LC is a homodimer that extends the IC's dimerization interface.

Absence of the mammalian dynein intermediate and light chains increases heavy-chain ATPase activity, reduces microtubule gliding activity, and causes overall structural instability (Gill *et al.*, 1994; Kini and Collins, 2001; King *et al.*, 2002). Recent work reconstituting the human cytoplasmic dynein complex from individually purified components found that the dynein heavy chain was unstable and aggregated in the absence of accessory chains and was monomeric when solubilized in high–ionic strength buffer (Trokter *et al.*, 2012). In the same study, addition of the dynein intermediate and light intermediate chains promoted heavy-chain dimerization. The addition of all accessory chains (IC, LIC, and LCs) was required to attain the motor's native conformation as determined by negative-stain electron microscopy (Trokter *et al.*, 2012). In rats, the IC–HC interaction has been roughly mapped to a 256-residue segment (amino acids 446–701) in the heavy chain's N-terminal region (Tynan *et al.*, 2000). In the mouse dynein heavy chain gene, a mutation in this segment, F580Y, results in a dramatic "legs at odd angles" (*Loa*) phenotype (Hrabé de Angelis *et al.*, 2000; Hafezparast *et al.*, 2003). The *Loa* mutation reduces motor velocity minimally but dramatically diminishes processivity (Ori-McKenney *et al.*, 2010). Collectively, mammalian dynein accessory chains and the heavy chain's N-terminal tail where they bind are implicated as critical determinants for dynein structure, dimerization, and processivity.

The *S. cerevisiae* dynein motor components Pac11 and Dyn2 have been implicated in Dyn1 stabilization and subcellular localization. Pac11 localizes Dyn1 to MT plus ends (Lee *et al.*, 2005) and, with Num1, anchors Dyn1 to the cortex for MT capture (Farkasovsky and Küntzel, 2001; Tang *et al.*, 2012). Pac11 and Dyn2 interact directly in vitro, as measured by mass spectrometry affinity capture (Ho *et al.*, 2002) and sedimentation equilibrium ultracentrifugation, and the two proteins colocalize in vivo (Stuchell-Brereton *et al.*, 2011). Dyn2 is predominantly a homodimer in solution and, like its higher eukaryotic counterparts, has been ascribed a functional role in mediating target dimerization (Romes *et al.*, 2012). The greater Dyn2/LC8 dynein light chain family binds diverse cellular factors in addition to the dynein motor complex (Rapali *et al.*, 2011). Dyn2/LC8 target-binding motifs span 11 amino acids and often contain a signature glutamine-threonine (QT) motif. An example of a nondynein Dyn2 target in *S. cerevisiae* is the nucleoporin Nup159, a cytoplasmic fibril component involved in gating nuclear export. Nup159 contains a pentameric Dyn2-binding array that recruits five Dyn2 homodimers, cross-linking and stabilizing the fibril structure (Stelter *et al.*, 2007). Pac11 contains two tandem Dyn2-binding sites, functionally homologous to the TcTex/LC8-binding sites in metazoan intermediate chains (Figure 1, A and B; Stuchell-Brereton *et al.*, 2011). The C-terminal Dyn2-binding site is reported to bind Dyn2 with higher affinity than the proximal N-terminal site, which favors cooperative binding once the C-terminal site is occupied (Stuchell-Brereton *et al.*, 2011). The Pac11 N-terminal region, including the two tandem Dyn2 sites, is monomeric in solution, but once bound to two Dyn2 homodimers, the two proteins form a $Pac11_2$-$(Dyn2_2)_2$ complex (Stuchell-Brereton *et al.*, 2011). How Pac11 and Dyn2 interact and regulate the Dyn1 motor is undetermined.

S. cerevisiae cytoplasmic dynein has emerged as a key model for structural (Carter *et al.*, 2011; Schmidt *et al.*, 2012), single-molecule (Reck-Peterson *et al.*, 2006; Gennerich *et al.*, 2007; Kardon *et al.*, 2009), and in vivo analyses of dynein motor mechanism and function (Li *et al.*, 2005; Moore *et al.*, 2008). Single-molecule assays have primarily probed the activity of the dynein heavy chain's motor domain. In contrast to their mammalian counterparts, the roles of dynein light and intermediate chains in yeast dynein activity have not been characterized by structural or single-molecule analyses. Here, we investigate the interaction between Dyn2 and Pac11 and probe the role of these accessory chains in dynein motor activity. We report the crystal structure of Dyn2 in complex with the second Pac11 Dyn2-binding site, determined to 1.9-Å resolution. We determine the affinity between Dyn2 and the second Pac11 Dyn2-binding site, characterize the determinants that confer Dyn2 dimerization and Pac11 binding, and show that the Dyn2-Pac11 complex enhances Dyn1 velocity, promotes Dyn1 homodimerization, and dramatically potentiates motor processivity.

RESULTS

Yeast Pac11 contains two conserved Dyn2-binding motifs

To compare and contrast the structural features of dynein intermediate chains from yeast with those from higher eukaryotes, we mapped the domain architecture of *S. cerevisiae* Pac11 and human

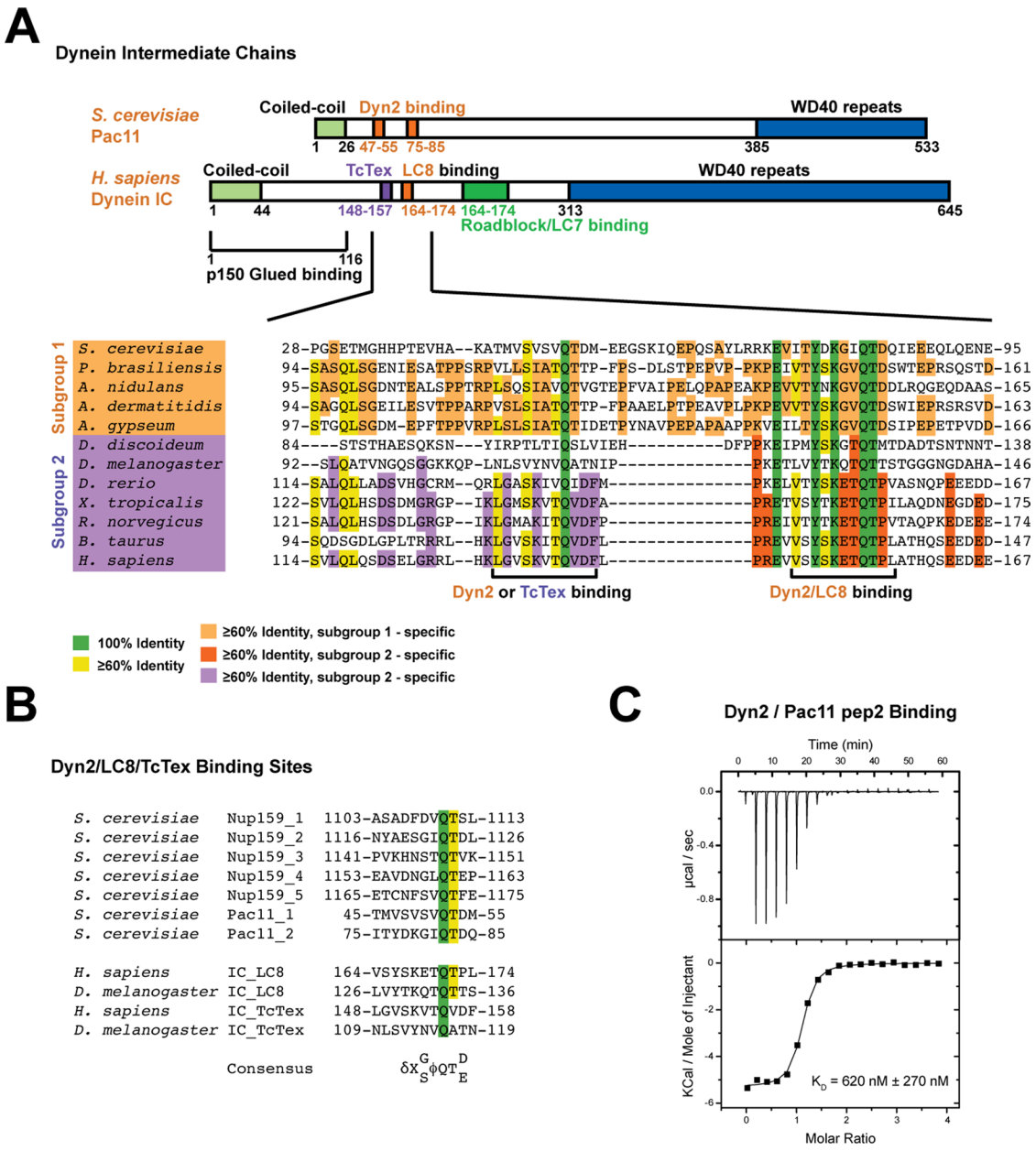

FIGURE 1: Dynein ICs contain conserved dynein LC-binding motifs near the predicted N-terminal coiled-coil domain. (A) Domain diagrams of dynein intermediate chains from *S. cerevisiae* and *Homo sapiens* consisting of a conserved, predicted N-terminal coiled-coil region followed by arrayed dynein LC-binding sites. The *S. cerevisiae* dynein IC contains two Dyn2-binding sites, whereas the human counterpart contains sequential binding sites for the light chains TcTex, LC8, and LC7. The Dyn2- and LC8-binding sites contain the invariant, signature QT motif. The ICs also contain C-terminal WD40 repeats predicted to form a β-propeller structure. The *H. sapiens* IC contains a $p150^{Glued}$-binding site between residues 1 and 116. A sequence alignment across 12 species is shown below with identity contoured at 100% (green) and ≥60% (yellow) across all species shown. Two subgroups were delineated: subgroup 1 comprising *S. cerevisiae*, *Paracoccidioides brasiliensis*, *A. nidulans*, *Ajellomyces dermatitidis*, and *Arthroderma gypseum* with two known or predicted Dyn2/LC8-binding sites; and supgroup 2, comprising *Dictyostelium discoideum*, *Drosophila melanogaster*, *Danio rerio*, *Xenopus tropicalis*, *Rattus norvegicus*, *Bos taurus*, and *H. sapiens* with known or predicted sequential TcTex- and LC8-binding sites. Within these subgroups, 60% identity is highlighted in light orange (subgroup 1) or purple (subgroup 2, TcTex site) and dark orange (subgroup 2, LC8 site). (B) Reported Dyn2 binding sites in *S. cerevisiae* Nup159 and Pac11 aligned with the LC8- and TcTex-binding sites from human and *Drosophila* dynein ICs. The Dyn2/LC8-binding sites display a highly conserved QT sequence motif that is QV in the *H. sapiens* IC TcTex-binding site and QA in the *Drosophila* site. A general consensus sequence is indicated below, where δ is a charged residue, X is any residue, and φ is V, L, or I. (C) Pac11 pep2 binds Dyn2 exothermically in a 2:2 (modeled as a 1:1) stoichiometry with K_d = 620 ± 270 nM as measured by isothermal titration calorimetry. Top, heat generated by sequential 19 × 2 µl injections of 1 mM Pac11 pep2, injected into the ITC cell containing 200 µl of 50 µM Dyn2. Bottom, data fit to a single-binding-site model from one of three independent experiments with averaged K_d (± SD).

dynein IC (Figure 1A). Higher eukaryotic dynein ICs contain a predicted N-terminal coiled-coil domain followed by three sequential dynein LC–binding sites for TcTex, LC8, and LC7, respectively. Although mammalian IC–LC interactions have been biophysically and structurally characterized, a molecular and structural analysis of yeast dynein IC–LC interactions is incomplete. We created a sequence alignment of dynein ICs, spanning the first two LC-binding sites across diverse yeast species, as well as in higher eukaryotes (Figure 1A). Yeast contains a solitary dynein LC, Dyn2, which is homologous to LC8. Previous work identified two Dyn2-binding sites in the Pac11 IC (Stuchell-Brereton *et al.*, 2011). Each binding site contains a signature LC-binding motif characterized by sequential QT residues. The first Dyn2-binding site substitutes for the corresponding TcTex-binding site in higher eukaryotes, whereas the second Dyn2-binding site is homologous to the higher eukaryotic IC LC8-binding site. The TcTex-binding site displays moderate homology to Dyn2/LC8-binding sites. TcTex and LC8/Dyn2 share a similar fold and target-binding mode, but TcTex is elongated relative to LC8, and the two families have little sequence homology (Williams *et al.*, 2005). The two tandem Pac11 Dyn2-binding sites are conserved across other yeast species (Figure 1A). Dyn2-binding sites characterized in *S. cerevisiae* proteins include a pentameric Dyn2-binding array present in the nucleoporin Nup159, where Dyn2 is believed to promote Nup159 oligomerization (Stelter *et al.*, 2007) and scaffold extension of the cytoplasmic fibril to effectively gate nuclear transport. We aligned the Pac11 and Nup159 Dyn2-binding sites, which highlights the invariant QT motif. Although residues flanking the QT motif exhibit variance, a general consensus sequence is evident: δ-X-G/S-φ-Q-T-D/E, where δ is a charged residue, X is any residue, and φ is V, L, or I (Figure 1B).

Dyn2 binds Pac11 site 2 with submicromolar affinity

To determine the affinity between Dyn2 and the individual Pac11 Dyn2-binding sites, we performed isothermal titration calorimetry (ITC). Two peptides, each corresponding to the Pac11 Dyn2-binding sites, were synthesized and designated Pac11 pep1 and pep2, respectively. Pac11 pep1 proved insoluble, likely due to its high hydrophobic content, and precluded further investigation. Pac11 pep2 was solubilized and injected into the ITC cell containing Dyn2 at pH 6.8 (Figure 1C). Pac11 pep2 bound Dyn2 exothermically at 26 °C. To fit the data, we used a single-site binding model as used in other LC-binding studies (Radnai *et al.*, 2010; Romes *et al.*, 2012). The Dyn2 homodimer has two sites that bind peptides independently, enabling the 2:2 (Dyn2:peptide) interaction to be effectively modeled as a 1:1 interaction. The data were well described by a single-site binding model, yielding an average binding affinity K_d = 620 nM ± 270 nM (Figure 1C; N = 1.05 ± 0.02 sites, ΔH = –5175 ± 139 cal/mol, ΔS = 11.3 ± 1.5 cal/mol per deg). Previous Dyn2/LC8-binding experiments found that light chains bind peptides either endothermically or exothermically, depending on the peptide sequence (Hódi *et al.*, 2006; Wagner *et al.*, 2006; Benison *et al.*, 2008; Radnai *et al.*, 2010; Nyarko *et al.*, 2011; Rapali *et al.*, 2011; Romes *et al.*, 2012). Previous characterization of Dyn2-Nup159 interactions showed both thermal binding modes, with K_d = 13–18 μM (Romes *et al.*, 2012), indicating that the Pac11 pep2 interaction is an order of magnitude tighter than Dyn2-binding sites characterized to date. Mammalian LC8 binds similar-length peptides exothermically with K_d = 1 μM for the apoptosis regulator Bmf and 7 μM for neuronal nitric oxide synthase (Radnai *et al.*, 2010). Thus the Dyn2-Pac11 pep2 interaction is on par with known high-affinity LC8 interactions. Although the Pac11 N-terminal region contains a predicted coiled coil, previous analytical ultracentrifugation studies indicated that this region is unlikely to confer Pac11 homodimerization in the absence of Dyn2 (Stuchell-Brereton *et al.*, 2011) (a coiled coil may form, however, once Dyn2 mediates initial Pac11 dimerization). Because the $Pac11_2$-$(Dyn2_2)_2$ complex is formed through multivalent interactions, the measured Dyn2 affinity for Pac11 pep2 is likely weaker than its affinity for native Pac11.

Structure of the Dyn2-Pac11 complex

To determine the molecular architecture of the Pac11-Dyn2 complex, we crystallized Dyn2 in complex with Pac11 pep2. Dyn2:Pac11 pep2 crystals were obtained from a solution containing a 1:1.2 M ratio of Dyn2 and Pac11 pep2. A complete diffraction data set was collected to 1.90-Å resolution in space group $C222_1$. The structure was solved by molecular replacement using a single Dyn2 chain derived from the Dyn2-Nup159 structure (PDB 4DS1; Romes *et al.*, 2012). Clear electron density for all Pac11 pep2 chains was evident in the molecular replacement electron density map ($F_o - F_c$), confirming the presence of bound peptide. The structure was built and refined to R and R_{free} factors values of 16.0 and 21.2, respectively, and is presented in Figure 2A. Multiple Dyn2-Pac11 complexes were present in the asymmetric unit, and each yielded a similar structure (Figure 2B; root-mean-square deviation, 0.18 Å across 168 Cα atoms) indicative of a relatively rigid, locked complex. Crystallographic data, refinement, and model statistics are presented in Table 1. A final, refined $2F_o - F_c$ electron density map for Pac11 pep2 is shown in Figure 2C.

The Dyn2 homodimer induces parallel homodimerization of Pac11 pep2 chains

In the Dyn2-Pac11 pep2 complex, two Pac11 chains form β-strands that symmetrically extend the central β-sheets of the Dyn2 homodimer (Figure 2A). Each β-sheet is composed of six antiparallel β-strands: four from one Dyn2 subunit, a fifth from the dimeric Dyn2 mate (features of which are designated with a prime symbol), and the sixth from one of the Pac11 pep2 strands, ordered β1-β4-β5-β2-β3′-Pac11 pep2. The two core β-sheets, related by a twofold symmetry axis, form a β-sandwich, flanked by Dyn2 helices α1 and α2. The α2 helix lines one side of the Pac11 pep2-binding site. The two Pac11 peptides in the complex are positioned parallel to one another on opposite sides of the Dyn2 homodimer. The distance between equivalent residues in each of the two Pac11 peptides (as measured between Cα carbon atoms) varies from 14 to 22 Å. Thus, within Pac11's LC-binding region, the Dyn2 homodimer drives parallel Pac11 dimerization. This structural arrangement is consistent with an N-terminal parallel coiled coil in Pac11.

Dyn2 engages Pac11 pep2 using extensive hydrogen bonding, van der Waals contacts, and canonical QT-motif recognition determinants

Pac11 pep2 residues Y76–Q82 form a β-strand running antiparallel to Dyn2-β3 (Figure 2A). Pac11 pep2 binds the Dyn2 homodimer through standard antiparallel β-sheet hydrogen bonding, as well as via distinct side-chain interactions that engage both Dyn2 subunits in the homodimer (Figure 3, A and B). The largest number of hydrogen bonds and van der Waals contacts are contributed by the canonical LC8 target motif determinants, Pac11 pep2 residues Q82 and T83 (Figure 3C). Overall, the number of hydrogen bonds and van der Waals interactions likely contribute to both the stability and specificity of the Dyn2-Pac11 pep2 interaction. Dyn2 recognizes similar target determinants in Nup159 (Supplemental Figure S1) and binds Nup159 in an analogous, antiparallel β-strand configuration (Romes *et al.*, 2012). To compare and contrast LC target binding

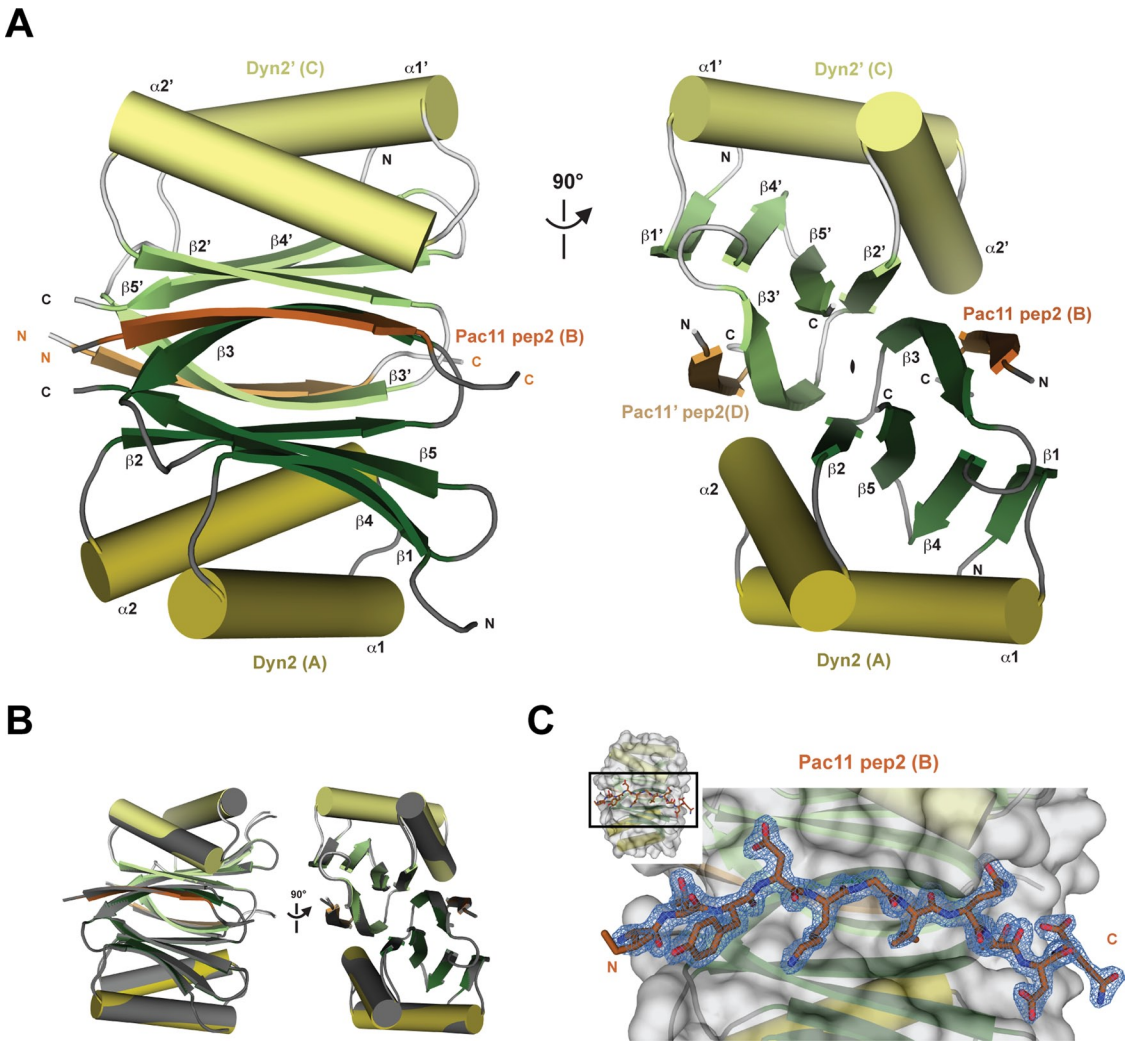

FIGURE 2: The structure of the Dyn2-Pac11 pep2 complex shows a Dyn2 homodimer bound to two Pac11 pep2 chains that form flanking, symmetric β-strands on the core composite Dyn2 β-sandwich. (A) Structure of the Dyn2-Pac11 pep2 tetrameric structure shown in cartoon format. Dyn2 chains are shown with β-strands in green, α-helices in yellow, and loops in gray; Pac11 chains are colored orange. Dyn2 chain A and Pac11 pep2 chain B are shown in darker shades, Dyn2 chain C and Pac11 pep2 chain D are shown in lighter shades. The image at left is rotated 90° about the *y*-axis to generate the view shown at right, highlighting the twofold noncrystallographic symmetry operator about the *z*-axis that relates the two pairs of Dyn2-Pac11 pep2 chains in the complex. Primes designate components of the homodimeric mate. (B) Dyn2 (chain E) and Pac11 pep2 (chain F) form a tetrameric complex ($Dyn2_2$-$Pac11\ pep2_2$) via crystal symmetry. The two Dyn2-Pac11 pep2 complexes—one comprising chains A–D related through noncrystallographic twofold symmetry (colored and oriented as in A) and the second generated through a crystallographic twofold relating chains E and F with E′ and F′ (colored dark gray)—align with a root-mean-square deviation across 168 common Cα atoms equal to 0.182 Å, indicating that Dyn2 forms a rigid complex with Pac11 pep2. (C) Stick diagram of Pac11 pep2 (dark orange) bound in the homodimeric Dyn2-binding cleft (gray surface on top of cartoon), oriented as in A (image at left). The $2F_o - F_c$ electron density for Pac11 pep2 is shown in blue mesh, contoured at 1.0 σ. Inset shows area in zoom view.

determinants across species, we defined the target QT motif glutamine as a zero reference point and numbered residues N- and C-terminal to it negative and positive, respectively. We note specific peptide-binding determinants in Dyn2 targets that contrast with equivalent positions in higher eukaryotic LC8 targets. Specifically, Dyn2 recognizes a glycine at position –2 in both Pac11 pep2 and Nup159 pep2 (Figures 1B and 4, A and B, and Supplemental Figure S1). Across known Dyn2 targets, the –2 position is predominantly occupied by a glycine or serine residue. This pattern is maintained across dynein ICs from diverse yeast species. The LC-binding sites in yeast ICs contain a glycine, alanine, or serine at position –2 (Figure 1, A and B). This contrasts with the bulkier side chains (commonly glutamate or glutamine) at position –2 in higher eukaryotic LC-binding sites. In yeast Dyn2, a bulky arginine side chain projects from the flanking α2 helix to interact with the target glycine at position –2. In contrast, in *Drosophila*, a less bulky lysine residue (K36) occupies the position equivalent to the yeast arginine, leaving space for a glutamine at target position –2 (Figure 4, A–D).

An F76K/Y78E double mutation in the Dyn2 peptide-binding site abrogates Pac11 pep2 binding

To confirm the role of Dyn2 target-binding determinants observed in our crystal structure, we mutated two residues at the Pac11 pep2-binding site and examined the effect on Pac11 binding. Residues

Data collection	
Wavelength (Å)	0.97920
Space group	$C222_1$
Cell dimensions *a*, *b*, *c* (Å)	101.5, 112.7, 56.4
Resolution (Å)	50.0–1.90 (1.97–1.90)
Number of reflections: measured/unique	117,213/25,589
Completeness (%)	98.5 (88.8)
Mean redundancy	4.6 (3.6)
$<I/\sigma>$	15.5 (2.5)
R_{sym}	0.09 (0.41)
Refinement	
Resolution (Å)	37.7–1.90 (1.97–1.90)
R/R_{free} (%)	16.0 (19.9)/21.2 (27.0)
Number of reflections, R/R_{free}	23,575 (2089)/2000 (178)
Total atoms: protein/water	2343/274
Stereochemical ideality (rmsd): bonds/angles (Å/deg)	0.007/1.04
Mean *B*-factors (Å^2): main chain/side chain/water	15.7/24.5/20.6
B-factor rmsd (Å^2): main chain/side chain	2.1/4.4
Ramachandran analysis: favored/allowed (%)	97.8/2.2

Parentheses give statistics for the high-resolution shell; rmsd, root-mean-square deviation.
$R_{sym} = \Sigma_h \Sigma_i |I_i(h) - <I(h)>| / \Sigma_h \Sigma_i I_i(h)$, where $I_i(h)$ is the integrated intensity of the *i*th reflection with the Miller Index *h* and $<I(h)>$ is the average over Friedel and symmetry equivalents.
$R = \Sigma (|F_{obs}| - k|F_{calc}|) / \Sigma |F_{obs}|$.
R_{free} is calculated using a 7.8% subset of the data that are removed randomly from the original data and excluded from refinement.

TABLE 1: Data collection and refinement statistics.

F76 and Y78, located on the Dyn2 β4 strand, form extensive van der Waals contacts with Pac11 pep2 (Figures 3B and 5A). To abrogate the interaction with Pac11 pep2, we introduced charged residues at the Dyn2 positions F76K and Y78E, each designed to repel the local charged residues on Pac11 pep2: K79 and D84, respectively (Figure 5A). To ensure that these mutations did not affect Dyn2 homodimerization, we performed size exclusion chromatography and multiangle light scattering (SEC-MALS) on Dyn2 wild-type (WT) and F76K/Y78E constructs. Purified WT Dyn2 eluted as a homodimer, confirming previous analyses of Dyn2 and LC8 (Supplemental Figure S2; Liang *et al.*, 1999; Romes *et al.*, 2012). Dyn2 F76K/Y78E also eluted as a homodimer, although smaller peaks with larger calculated molecular weights were also observed, indicating a higher-order oligomeric subspecies. Because the major pool of Dyn2 F76K/Y78E was a homodimer, we used ITC to test whether the construct could bind Pac11 pep2. No binding between Dyn2 F76K/Y78E and Pac11 pep2 was observed across a span of component concentrations (Figure 5C and Supplemental Figure S3, A–C; see *Materials and Methods*). This finding supports the role of F76 and Y78 in Pac11 pep2 binding, as observed in our Dyn2-Pac11 crystal structure.

An H58K mutation in the Dyn2 dimerization interface abrogates dimerization and target peptide binding

Residues from each of the Dyn2 molecules in the homodimer comprise the Pac11 peptide-binding site. To test whether dimerization is required for target binding, we analyzed residues at the dimerization interface that could be mutated to prevent dimerization. An LC8 mutation, H55K, was reported to transform LC8 from a homodimer to a monomer (Nyarko *et al.*, 2005). The equivalent residue in Dyn2, H58, resides at the dimer interface, stacked 5.4 Å from its dimeric mate (H58′; Figure 5D). We mutated Dyn2 H58 to lysine and analyzed the oligomeric state of the mutant using SEC-MALS (Figure 5B). In contrast to homodimeric WT Dyn2 (Supplemental Figure S2), Dyn2 H58K eluted primarily as a monomer (Figure 5E). To determine whether monomeric Dyn2 can bind Pac11 pep2, we performed ITC using the Dyn2 H58K mutant. No binding between Dyn2 H58K and Pac11 pep2 was observed using a range of Dyn2 and Pac11 pep2 concentrations. These results indicate that Dyn2 homodimerization is required for target binding (Figure 5E and Supplemental Figure S3, B, D, and E). Collectively, Dyn2 is a homodimer, Dyn2 homodimerization is required for Pac11 binding, and Pac11 pep2 binds in the composite groove formed by Dyn2 homodimerization (as observed in our Dyn2-Pac11 pep2 crystal structure). Mutations in Dyn2's peptide-binding site or dimerization interface disrupt Pac11 pep2 binding.

Dyn2/Pac11 facilitates dynein single-molecule processivity

The results of our structural and biochemical investigations of the Dyn2-Pac11 interaction imply a role for Dyn2 in Pac11 dimerization. To investigate whether Dyn2-mediated Pac11 dimerization plays a role in the oligomerization of the dynein heavy chains and the dimerization-dependent motile single-molecule properties (velocity and processivity), we created strains in which either the *dyn2* gene or both the *dyn2* and *pac11* genes were deleted, respectively. Previous single-molecule experiments with full-length dynein labeled at its C-terminus with the HaloTag and covalently bound to tetramethylrhodamine (TMR) demonstrated that single Dyn1 motors containing both subunits are highly processive (take multiple steps along MT filaments without detaching) with an average run length of 1.7 µm (Reck-Peterson *et al.*, 2006).

We used a custom-built total internal reflection fluorescence (TIRF) microscope and performed kymograph analyses to determine the average velocities and run lengths of single dimeric Dyn1 molecules in the presence and absence of Dyn2 (*dyn2*Δ) and Dyn2/Pac11 (*dyn2*Δ*pac11*Δ), respectively. Dyn1 was C-terminally tagged with a HaloTag and site-specifically labeled with TMR. We performed experiments under decreased ionic strength (in dynein motility buffer [DMB]; see *Materials and Methods*) to enhance the detection of changes in run length of the Dyn1 motor purified from WT, *dyn2*Δ, and *dyn2*Δ*pac11*Δ strains with sufficient precision (preventing significant underscoring of short runs that occur within the detection limit of the microscope). Under these conditions, the velocities of Dyn1 motors purified from *dyn2*Δ and *dyn2*Δ*pac11*Δ strains were slightly decreased (113 and 118 nm/s respectively, $p < 0.0001$) compared with the 133-nm/s velocity of WT dynein (Figure 6, A and B). Surprisingly, when we analyzed motor processivity, we noted that Dyn1 molecules purified from *dyn2*Δ and *dyn2*Δ*pac11*Δ strains move significantly shorter distances (1.25- and 1.24-µm average run lengths, respectively) compared with the average 2.2-µm run length of WT dynein (Figure 6, A and C). These results demonstrate that Dyn2/Pac11 affect dynein processivity significantly and that loss of Dyn2 has similar effects to loss of both Dyn2 and its binding partner, Pac11. To investigate why the single and

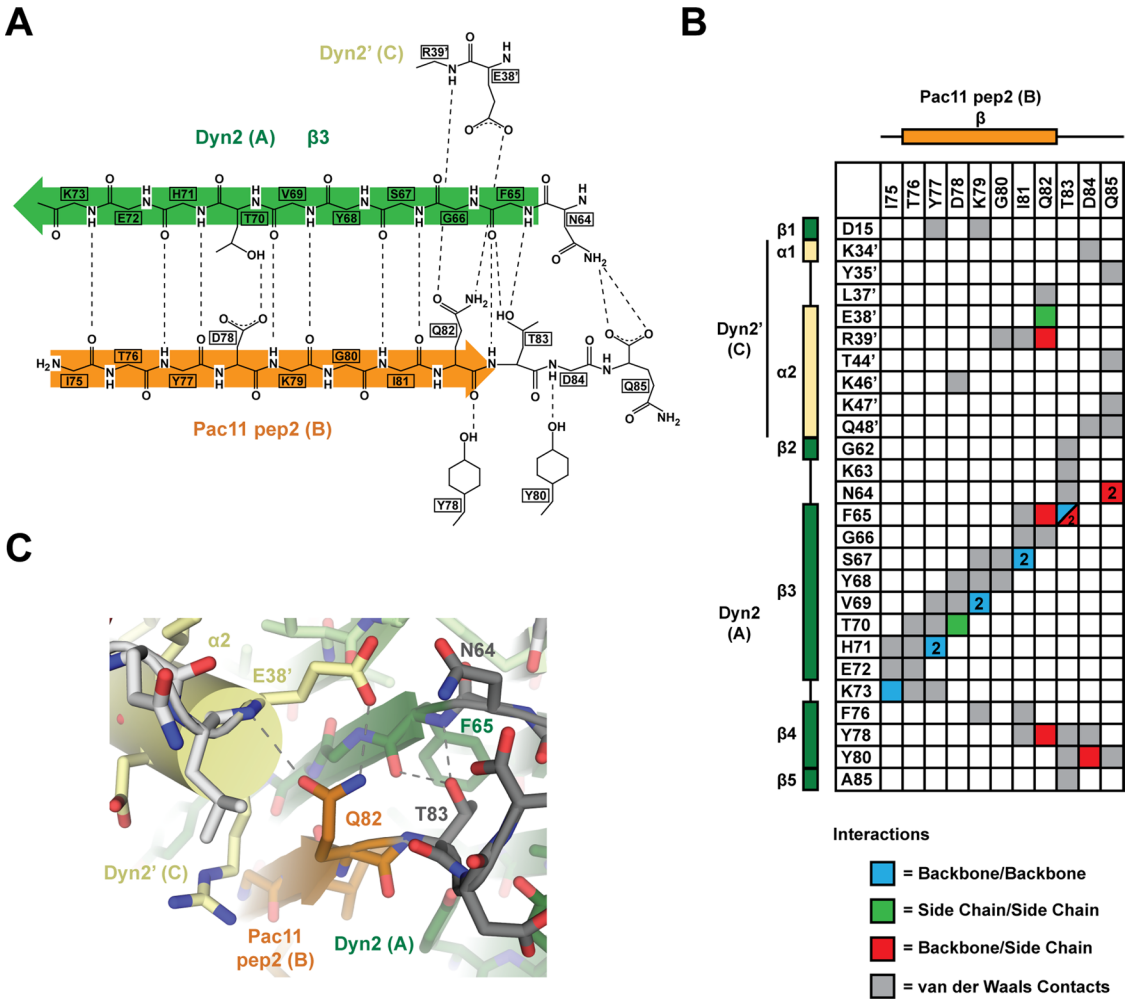

FIGURE 3: The Dyn2 homodimer interacts with Pac11 pep2 across an extensive hydrogen-bonding network that comprises antiparallel backbone/backbone β-strand interactions, as well as hydrogen bonding and van der Waals contacts that involve side chains. (A) A two-dimensional diagram of the hydrogen-bonding network (distances ≤3.5 Å, dashed lines) between Pac11 pep2 chain B (orange) and Dyn2 chains A and C (green). (B) Interaction matrix between Pac11 pep2 chain B (*x*-axis) and Dyn2 chains A and C (*y*-axis). Secondary structure is indicated along the axes (colored as in Figure 3A), as are residues involved in the interactions and their respective chain labels. Hydrogen bond interactions are delineated as backbone/backbone (blue), side chain/side chain (green), and backbone/side chain (red). The number of hydrogen bonds that occur between two residues is one unless otherwise noted by a 2 in the cell, indicating two hydrogen bonds occurring between these residues. Van der Waals contacts are indicated in gray (≤4.5 Å). Where more than one type of interaction occurs, the cell is split diagonally, with each half colored accordingly. (C) Stick diagram of the Pac11 pep2 QT motif (Q82, T83), highlighting the hydrogen-bonding network (dashed lines) these residues use to engage both Dyn2 homodimer subunits. Primes designate components of the homodimeric mate.

double deletions have very similar effects on dynein processivity and velocity, we next performed Western blot analysis to reveal differences in the amount of Pac11 that copurifies with the dynein HC in the presence and absence of Dyn2 (Figure 7A). This analysis revealed that the absence of Dyn2 dramatically reduces the relative amount of Pac11 that copurifies with the dynein HC (Figure 7A), suggesting that Dyn2 promotes the Pac11-Dyn1 interaction and that the loss of Dyn2 reduces stable Pac11-Dyn1 complex formation. Western blot analysis reflects an initial motor concentration of 80 nM. TIRF assays were performed after diluting motors to ~1 nM, which would favor Pac11-Dyn1 dissociation. To further test this idea, we performed multicolor single-molecule fluorescence analysis to probe for Pac11-Dyn1 complex formation under the conditions used in our single-molecule motility studies. In agreement with our hypothesis, Dyn1 purified from the WT strain shows significant colocalization between TMR-tagged Dyn1 and Cy5-labeled anti-Myc antibodies (which targets Myc-tagged Pac11), whereas Dyn1 purified from the *dyn2*Δ (or *dyn2*Δ*pac11*Δ) strain did not reveal any associated Pac11 (Figure 7B; see also Supplemental Figure S4 and Supplemental Materials and Methods for details underlying this analysis). Thus loss of Dyn2 increases the dissociation of Pac11 from Dyn1, which explains why motors purified from *dyn2*Δ and *dyn2*Δ*pac11*Δ strains behave similarly.

Dyn2/Pac11 help to maintain dynein heavy chains in a dimeric motile state

It was recently demonstrated that the *Loa* mutation (F580Y) in the mammalian dynein heavy chain's IC-binding site results in decreased motor run length (Ori-McKenney *et al.*, 2010). Of interest, brain cytosol from *Loa*$^{-/-}$ mice contains a greater fraction of free IC than in

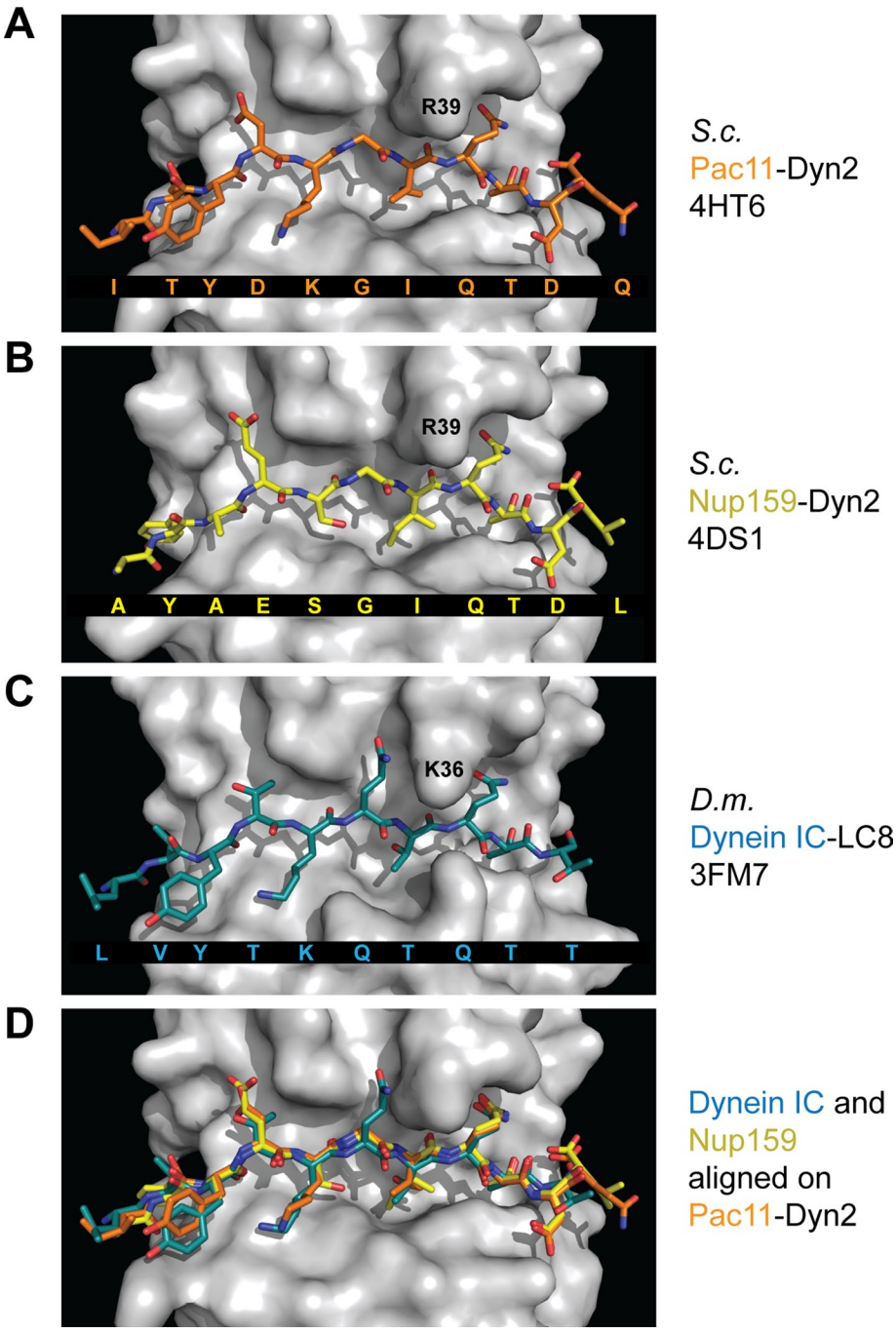

FIGURE 4: The Dyn2/LC8 target-binding cleft engages peptides similarly, capturing conserved site-specific determinants surrounding the QT motif while accommodating sequence variability in the flanking regions. (A–C) Structures of peptides (stick format) bound to dynein light-chain homodimers shown in surface representation. Shown are the yeast Pac11-Dyn2 complex (A; this work, PDB 4HT6), the yeast Nup159-Dyn2 complex (B; PDB 4DS1), and the *Drosophila* dynein IC-LC8 complex (C; PDB 3FM7). Peptide sequences are shown below each structure. (D) Overlay of the peptides shown in A–C after structurally aligning their bound dynein light chains using the Dali pairwise alignment server. Only the Dyn2-binding cleft from the Pac11-Dyn2 complex is shown for simplicity. Peptides are colored as in A–C.

WT (determined via sucrose density gradient centrifugation analysis), suggesting a correlation between dynein processivity and the presence/absence of bound IC (Ori-McKenney *et al.*, 2010). Because heavy-chain dimerization is required for processive motion (the "walking" of dynein along MTs requires two motor domains ["heads"]; Reck-Peterson *et al.*, 2006), we hypothesized that the Dyn2-Pac11 complex helps to maintain Dyn1 in a homodimeric, motile state. To determine whether there is a population of monomeric motors and examine monomeric motor activity at the single-molecule level, we analyzed the fluorescence intensities of the purified motors in our single-molecule TIRF assay (Figure 8, A–C, and Supplemental Table S2). Because dynein dimers are expected to have at most two TMR molecules bound (the labeling efficiency is ~65%; see legend to Figure 8B), whereas a monomer is expected to have no more than one TMR bound, we can distinguish between monomeric, immobile and dimeric, motile states of dynein by analyzing the intensities associated with motile versus immobile motors (see arrows 1–3 and corresponding intensity distributions, Figure 6A). In agreement with our hypothesis, ~65% of motile motors exhibit a fluorescence intensity that corresponds to a maximum of two dyes (Figure 8B), whereas the majority of immobile motors show single-dye fluorescence (Figure 8C). Of note, the fraction of motile motors decreased from 60 to 30% as a result of Dyn2 and Pac11 deletion (Figure 8A). The decrease in the fraction of motile motors from the *dyn2Δ* and *dyn2Δpac11Δ* strains correlates with an increase of the fraction of immobile, MT-bound fluorescent spots containing predominantly one dye (Figure 8C) and an increasing number of bright fluorescent spots bound to the coverslip surface containing more than two dyes (Supplemental Figure S5). These correlations suggest that the loss of the Dyn2-Pac11 complex promotes Dyn1 monomerization and aggregation, which agrees with previous studies on mammalian dynein that showed that IC removal resulted in decreased heavy-chain stability (Gill *et al.*, 1994; King *et al.*, 2002; Trokter *et al.*, 2012).

DISCUSSION

Many single-molecule dynein experiments examined the dynein motor domain fused to an artificial dimerization domain that ensures motor domain homodimerization, a critical prerequisite for processivity (Reck-Peterson *et al.*, 2006; Numata *et al.*, 2011). Although this facilitates robust analysis of motor domain function, it excludes analysis of any role the heavy chain's N-terminal domain and its associated binding partners may play in dynein motor domain activity. The dynein heavy-chain N-terminal domain and its associated chains are highly conserved from yeast to humans, suggesting a key functional role in the motor complex. Here, we marshaled biochemical, structural, and single-molecule analyses to probe the role of the light and intermediate chains in the dynein motility mechanism.

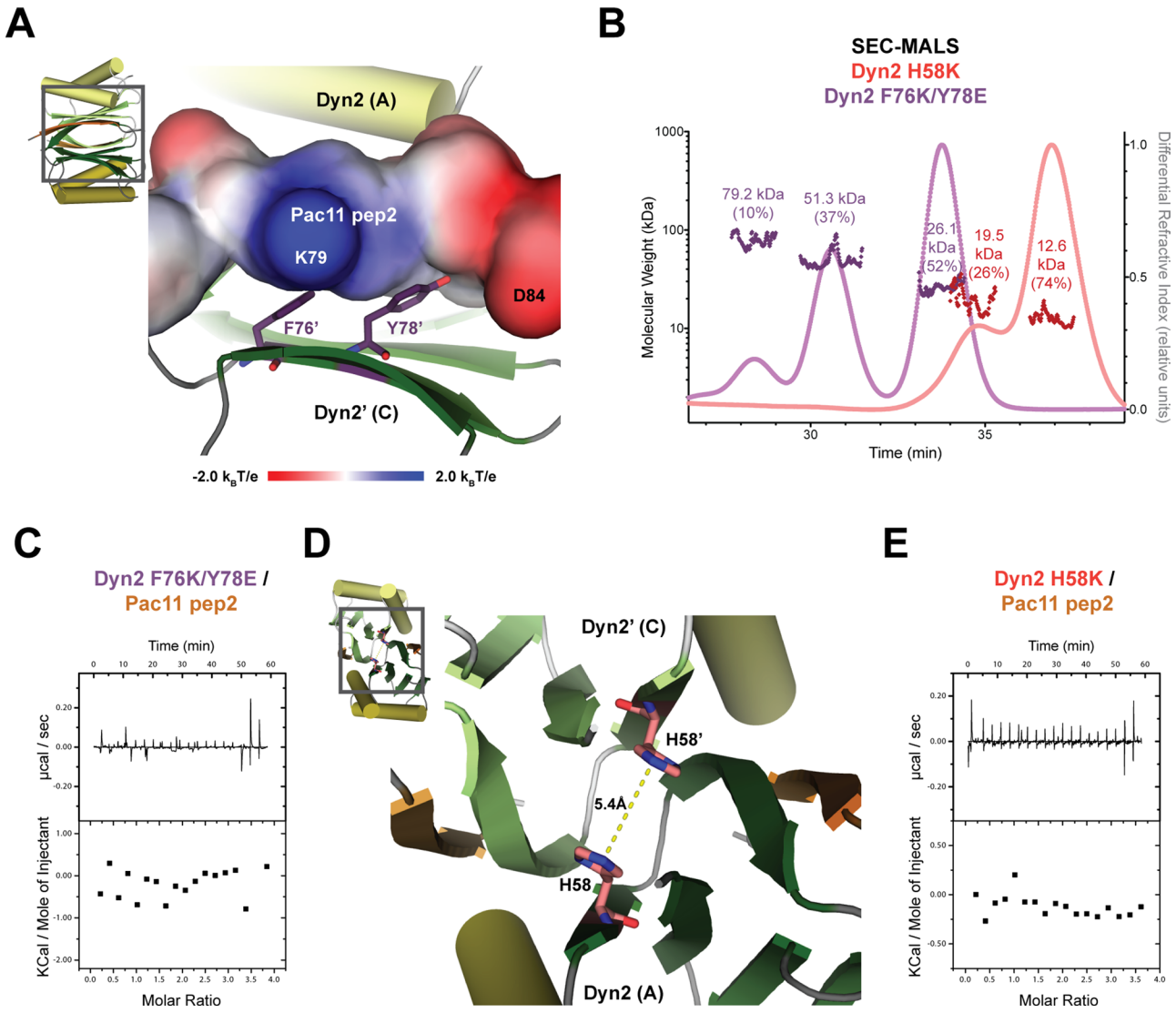

FIGURE 5: The ability of Dyn2 to bind Pac11 pep2 and homodimerize is abrogated through key mutations. (A) The crystal structure of Dyn2 in cartoon format (colored as in Figure 3A) with electrostatic surface potential indicated for the Pac11 pep2 chain contoured from −2.0 (red) to +2.0k_BT/e (blue). Two residues from the Dyn2 chain A β4 strand, F76 and Y78 (shown in stick format, colored purple), interact with Pac11 pep2. Primes designate components of the homodimeric mate. (B) SEC-MALS analysis of the Dyn2 mutants F76K/Y78E and H58K. Individual 50-µl injections of 6 mg/ml Dyn2 F76K/Y78E mutant (fuchsia, dark purple) and 10 mg/ml Dyn2 H58K mutant (pink and red traces) were analyzed at pH 6.8. The differential refractive index for each mutant was normalized to the tallest peak in that respective run (Dyn2 F76K/Y78E to the 26.1-kDa peak, Dyn2 H58K to the 12.6-kDa peak). Each peak shows the measured molecular weight (Dyn2 F76K/Y78E in dark purple, Dyn2 H58K in dark red) and the fraction of total injected mass in each peak (in parentheses). (C) Ability of the Dyn2 F76K/Y78E mutant to interact with Pac11 pep2 explored by ITC. Top, heat generated by 19 × 2 µl sequential injections of 1 mM Pac11 pep2 into the ITC cell containing 200 µl of 50 µM Dyn2 F76K/Y78E. No detectable Pac11 pep2 binding was observed. (D) The crystal structure of Dyn2 in cartoon format (colored as in Figure 3A), highlighting H58 and its dimeric mate, H58′, in stick format, colored pink, located at the twofold dimerization interface. The zoom window shows that the H58 and H58′ imidazole rings stack 5.4 Å apart across the twofold axis. (E) Ability of the Dyn2 H58K mutant to interact with Pac11 pep2 explored by ITC. Top, heat generated by sequential 19 × 2 µl injections of 1 mM Pac11 pep2 into the ITC cell containing 200 µl of 50 µM Dyn2 H58K. No detectable Pac11 pep2 binding was observed.

We find that Dyn2 binds Pac11's second Dyn2-binding site with an affinity of 620 nM. This interaction is one of the higher-affinity LC8/Dyn2 family-target interactions determined and our measurement likely underestimates the affinity between Dyn2 and full-length Pac11 due to the avidity effects of Dyn2 homodimers interacting with two Pac11 chains, each with dual, arrayed Dyn2-binding sites. Our structural analysis of the Dyn2-Pac11 pep2 complex shows a canonical Dyn2-target interaction, with the Dyn2 homodimer bound to two parallel Pac11 chains. Previous work analyzing the Pac11-Dyn2 interaction using analytical ultracentrifugation showed Dyn2-dependent Pac11 dimerization, yielding a complex mass on par with a $Pac11_2$-$Dyn2_4$ complex that, with our crystal structure, supports parallel Pac11 chains bridged at two sites by Dyn2 homodimers (Stuchell-Brereton *et al.*, 2011). This predicted $Pac11_2$-$(Dyn2_2)_2$

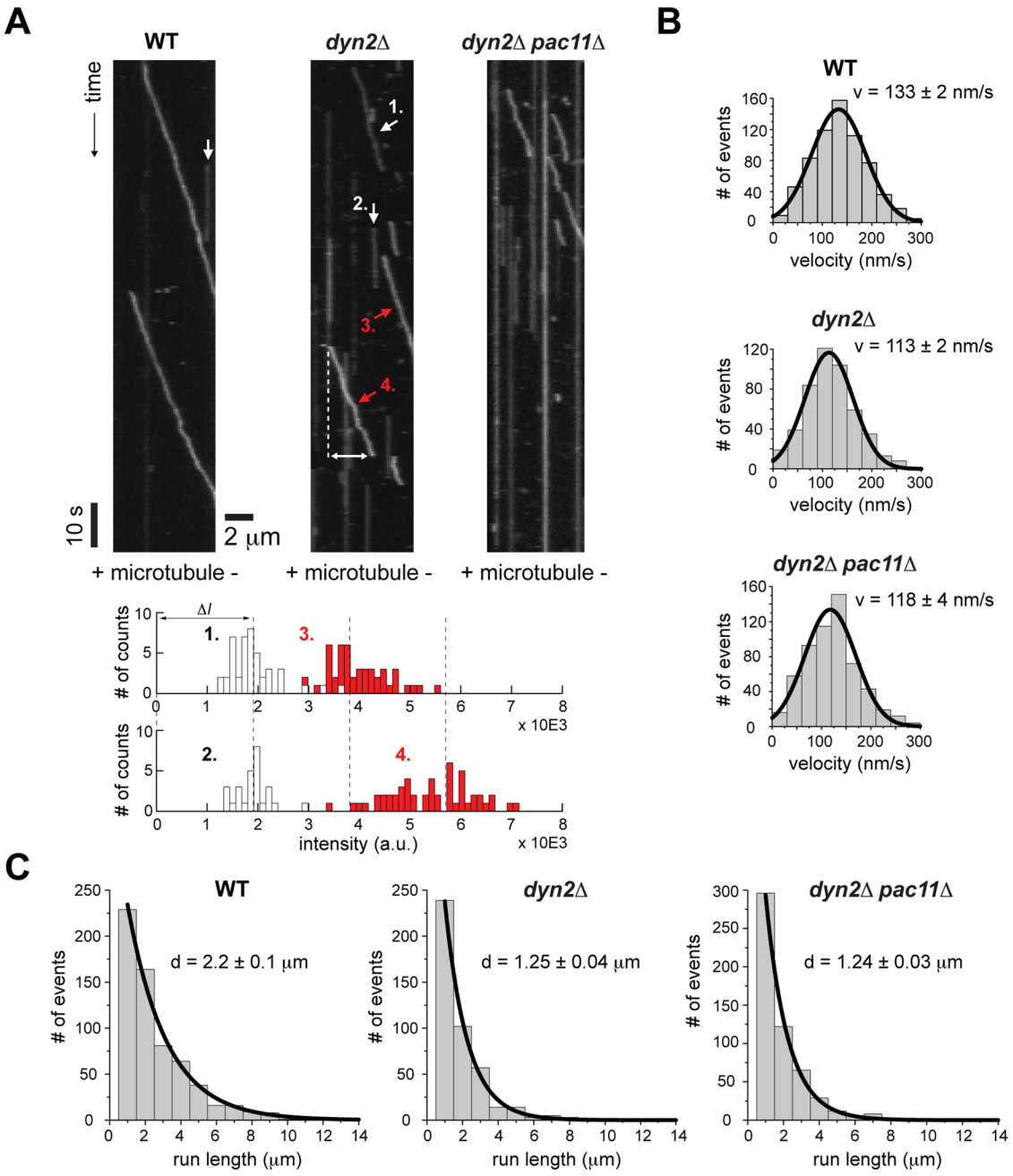

FIGURE 6: Dynein from *dyn2Δpac11Δ* cells shows decreased run lengths compared with motors purified from WT cells. (A) Kymographs were generated by stacking line scans along the long MT axis using custom-made analysis software (Supplemental Material and Methods). Diagonal lines represent moving molecules, with velocity equal to the inverse of the slope. The run length of individual molecules can be easily determined (double-headed arrow). An increasing number of stationary Dyn1 molecules can be seen (vertical lines) for Dyn1 purified from the deletion strains. Analysis of the fluorescence intensities (post background subtraction) reveals that moving and immobile Dyn1 molecules contain predominantly one or two TMR molecules and very rarely more than two dyes (example in bottom inset and statistics in Figure 8 and Supplemental Table S2). Pooling the two distributions with the lowest mean intensities (1 and 2) and taking the average of both means yields 1.9 a.u. (ΔI; note that when bleaching occurs during the image acquisition time, the lowest mean intensities in our kymograph-based intensity analysis show one-step photobleaching, confirming single-dye identity; Supplemental Figure S6A). Dashed lines are placed at integral multiples of ΔI, revealing that the two moving motors carry two and three dyes, respectively (3 and 4). The latter observation suggests the rare occurrence of a moving Dyn1 aggregate (see also Supplemental Figure S5). (B) Histograms of velocities ($v > 0$ nm/s) of single Dyn1 molecules at 1 mM ATP (WT, top; *dyn2Δ*, center; *dyn2Δpac11Δ*, bottom). Values are means ± SEM (n = 500–1000). (C) Histograms of run lengths of single Dyn1 molecules moving along MTs (WT, left; *dyn2Δ*, middle; *dyn2Δpac11Δ*, right). Values are means ± SEM (n = 500–1000).

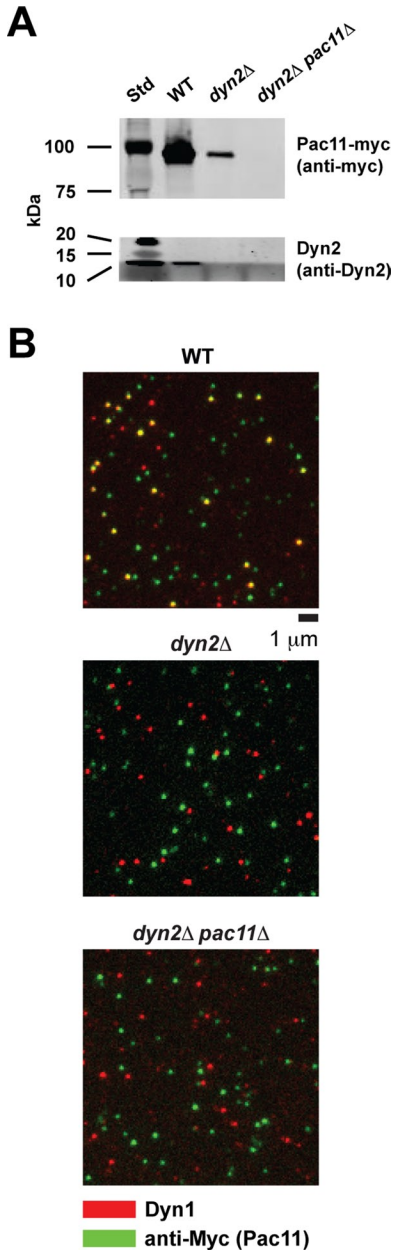

FIGURE 7: Absence of Dyn2 reduces Pac11-Dyn1 complex formation. (A) Copurification of Dyn2 and Pac11 with full-length Dyn1 through IgG affinity purification of cell lysate from WT, *dyn2*Δ, and *dyn2*Δ*pac11*Δ strains. Western blotting was performed with antibodies against Dyn2 (Stelter *et al.*, 2007) and against the Myc tag in Pac11. Subsequent SDS–PAGE and Western blot analysis confirms the absence of Dyn2 in the *dyn2*Δ and *dyn2*Δ*pac11*Δ deletion strains and the absence of Pac11 in *dyn2*Δ*pac11*Δ cells and reveals a significant reduction of Pac11 copurified with Dyn1 from *dyn2*Δ cells (for more details, see *Materials and Methods*). (B) TIRF-based, single-molecule fluorescence analysis confirms that the majority of TMR-labeled Dyn1 molecules purified from the WT strain are bound to Pac11-Myc, as revealed by the ~60% colocalization (yellow) of TMR-labeled Dyn1 (red) and Cy5-labeled anti-Myc antibodies (green) (top). In contrast, Dyn1 motors purified from the *dyn2*Δ (center) and *dyn2*Δ*pac11*Δ strains (bottom) do not show significant TMR-Cy5 colocalization (see Supplemental Materials and Methods for details underlying this analysis). Images represent 150 × 150–pixel subregions of the original 512 × 512–pixel EMCCD images (see Supplemental Figure S4 for larger field).

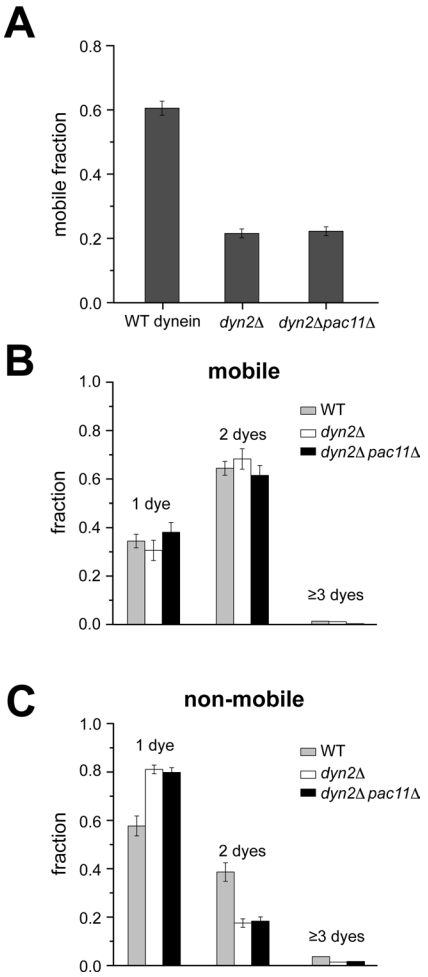

FIGURE 8: Single-molecule fluorescence analysis shows that Dyn2/Pac11 facilitate Dyn1 motility by promoting HC homodimerization. (A) Deletion of Dyn2 or both Dyn2 and Pac11 results in the same increase of the fraction of immobile Dyn1 molecules. (B) Analysis of the fluorescence intensities reveals that the majority of moving motors have two TMR-tagged Dyn1 heavy chains. The insignificant fraction of motile motors with more than two dyes (indicating higher oligomers) together with the negligible photobleaching (Supplemental Figure S6) allows the estimation of ~65% HC fluorescence labeling efficiency. (C) Analysis of the imaged fluorescence intensities reveals that the increased fraction of immobile Dyn1 in the absence of Dyn2 or both Dyn2 and Pac11 (A) is largely caused by HC monomerization, as indicated by the large fraction of immobile Dyn1 molecules with single-dye intensities. Note that not all Dyn1 motors purified from the WT and deletion strains are active and that the inactive, immobile motors purified from the WT strain have a higher likelihood to be dimers, which have a higher likelihood to be labeled with two dyes. Values are means ± SEM (see Supplemental Table S2 for corresponding data).

arrangement resembles the arrangement observed in crystal structures of the *Drosophila* IC_2-$TcTex_2$-$LC8_2$ complex (Williams *et al.*, 2007; Hall *et al.*, 2010). In these animal complexes, the TcTex light chain replaces the first Dyn2 binding site in yeast. Based on our affinity measurements and since Dyn2 is a homodimer, we predict that the $Pac11_2$-$(Dyn2_2)_2$ complex is highly stable and that Pac11 and Dyn2 work as a complex in dynein motor function. Our data show that the Pac11-Dyn2 complex promotes Dyn1 homodimerization and that loss of Dyn2 or Dyn2 and Pac11 enhances Dyn1 homodimer

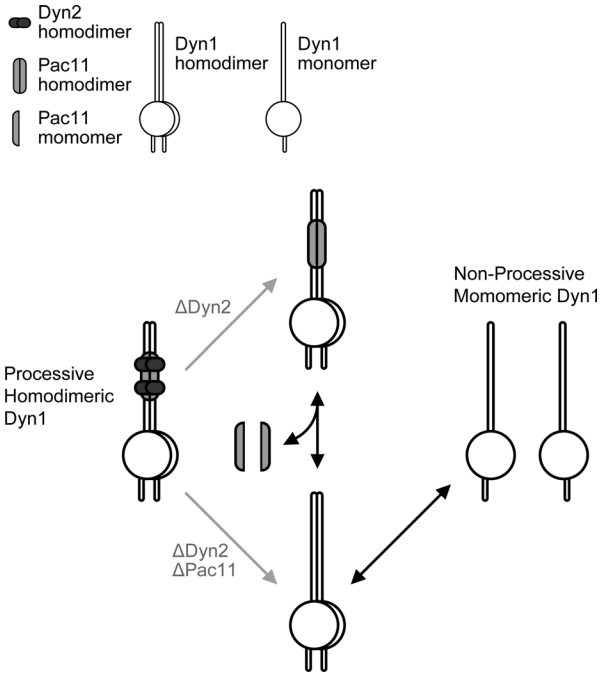

FIGURE 9: Model of Dyn2/Pac11-potentiated dynein heavy chain dimerization and concomitant motor processivity. The dynein heavy chain copurifies with Dyn2 and Pac11, yielding a highly processive motor. When Dyn2 and Pac11 are absent, the Dyn1 homodimer is more susceptible to monomerization, yielding nonprocessive motors. When Dyn2 is absent, less Pac11 copurifies with Dyn1, likely due to reduced affinity for the dynein heavy chain. If the Pac11-Dyn1 interaction is more labile, Dyn1 homodimers free of Pac11 can monomerize, yielding nonprocessive motors.

dissociation, leading to nonprocessive motors (Figure 9). How the $Pac11_2$-$(Dyn2_2)_2$ complex structurally interacts with the Dyn1 homodimer remains to be determined.

The Pac11-Dyn2 complex enhances Dyn1 homodimer stability, slightly increasing velocity and enhancing processivity significantly, likely by facilitating the alternating forward motions of dynein's two motor domains. Intriguingly, the IC-LC binding site overlaps the site of the mouse *Loa* mutation (F580Y) that causes neurodegenerative disease. Single-molecule experiments analyzing *Loa*-mutant dynein movement in vitro found increased lateral stepping and an increased ATP affinity, suggesting disrupted motor domain coordination that results in premature ATP binding in the rear head and subsequent release from the MT (Ori-McKenney *et al.*, 2010). *Loa* phenotypes show overlap with the behavior we observed for Dyn1 operating without Dyn2 or the Pac11-Dyn2 complex. Independent studies investigating whether the *Loa* mutation affects IC-HC complex stability found contrasting results, some showing decreased IC association (Ori-McKenney *et al.*, 2010) and others showing unaltered (Sivagurunathan *et al.*, 2012) or even increased IC association (Deng *et al.*, 2010). Whether absence of the IC-LC complex and the *Loa* mutation modulate HC activity through the same, overlapping, or independent mechanisms remains an open question. Nevertheless, in vivo analyses of phenotypes resulting from the *Loa* mutation provide insights that parallel our findings, such as decreased velocities and run lengths of vesicles transported by *Loa* dynein (Ori-McKenney *et al.*, 2010; Sivagurunathan *et al.*, 2012). Both the loss of the IC-LC complex and the *Loa* mutation suggest that key conserved elements in the HC N-terminal domain modulate motor domain activity. Additional evidence for the HC N-terminal domain exerting regulatory action on the motor domain comes from a recent study in *Aspergillus nidulans*, in which a F208V mutation in the dynein HC, located N-terminal to the IC-binding site, causes early endosomes to move less frequently and with a diminished velocity without affecting the HC-IC interaction (Qiu *et al.*, 2013). When the valine mutation was replaced with a bulkier hydrophobic side chain, isoleucine, WT vesicle motility was restored. The *A. nidulans* F208V mutation and the mouse *Loa* F580Y mutation both change the size of a hydrophobic residue. We suspect that these mutations alter the packing of the dynein N-terminal domain, each debilitating the regulatory action that this domain exerts on the motor domain. Additional support comes from reconstitution studies of human cytoplasmic dynein in which the addition of the IC and LIC promoted HC dimerization, and all accessory chains were required (including the LCs) for the motor complex to appear in its native conformation, as determined by negative–stain electron microscopy (Trokter *et al.*, 2012). Our results highlight commonality between mammalian and yeast cytoplasmic dynein. It is likely that the structure of the HC's N-terminal domain and its IC-LC–potentiated dimerization are critical for its regulatory action. Removal of the IC-LC complex or mutations within the HC N-terminal domain itself may therefore yield similar, yet distinct effects on HC motor activity. Future single-molecule studies will probe the role of the IC-LC complex in motor domain coordination using differentially labeled motor domains, as well as optical trapping to examine accessory-chain–dependent effects on force generation. Probing a direct interaction between the HC N-terminal tail and motor domain during active walking in the presence and absence of Dyn2/Pac11 awaits future single-molecule studies combined with Förster resonance energy transfer.

MATERIALS AND METHODS

Cloning, expression, and purification of full-length Dyn2

Full-length Dyn2 was cloned from *S. cerevisiae* S288c as described (Romes *et al.*, 2012). Briefly, Dyn2 was cloned into pGEX-6P2 (GE Healthcare, Piscataway, NJ), yielding an N-terminal, cleavable glutathione *S*-transferase (GST) tag. GST-Dyn2 was expressed in BL21 DE3 (pLysS) and induced using 0.1 mM isopropyl-1-thio-β-D-galactopyranoside at 18°C for 16 h. Cells were harvested, resuspended in lysis buffer, and lysed by sonication. Dyn2 was purified using a glutathione sepharose column, eluted, and incubated with PreScission protease (GE Healthcare) to cleave the GST tag. Final purification was performed using an SP Sepharose Fast Flow column (GE Healthcare). The Dyn2 peak was collected and exchanged into buffer A (50 mM NaCl, 25 mM 4-(2-hydroxyethyl)-1-piperazineethanesulfonic acid [HEPES], pH 6.8, and 0.1% β-mercaptoethanol). The final, purified Dyn2 protein was concentrated to 5 mg/ml, snap frozen in liquid nitrogen, and stored at –80°C. The final Dyn2 protein contained an N-terminal GPLGS cloning artifact.

Cloning, expression, and purification of Dyn2 mutants

Dyn2 H58K and F76K/Y78E mutagenesis was done using the QuikChange method (Stratagene, Santa Clara, CA) with the complementary oligonucleotides for the H58K mutant, 5′-GGATGTCAAATACGGCAATACCTGGAAAGTGATTGTCGGAAAGAACTTTGGG-3′ (where the underlined portion codes for the mutated codon) and 5′-CCCAAAGTTCTTTCCGACAATCACTTTCCAGGTATTGCCGTATTTGACATCC-3′; and the complementary oligonucleotides for F76K/Y78E, 5′-GTGACACACGAAAAGGGCCATAAAGTTGAATTCTATATCGGTCCACTGGCG-3′ and 5′-CGCCAGTGGACCGATATAGAATTCAACTTTATGGCCCTTTTCGTGTGTCAC-3′. Both the

single and double mutants were sequence confirmed. The expression and purification of Dyn2 H58K and Dyn2 F76K/Y78E followed the same protocols and buffers as described for WT Dyn2.

Pac11 peptide synthesis

Pac11 peptide 1 (pep1; YMVSVSVQTDM, residues 45–55) and peptide 2 (pep2; ITYDKGIQTDQ, residues 75–85) were synthesized at the University of North Carolina Microprotein Sequencing and Peptide Synthesis Facility. Peptide 1 was designed with an amino-terminal tyrosine in order to quantify the peptide concentration. Lyophilized peptides were added to buffer A. Peptide 1 proved insoluble in buffer A, and attempts to solubilize it in buffers containing increased salt, different pH ranges, or various detergents did not result in solubilization.

Crystallization

Final concentrations of 0.5 mM Dyn2 and 0.6 mM Pac11 pep2 were incubated in buffer A for 30 min at ambient temperature. Crystals were obtained by hanging-drop vapor diffusion using 2 µl of the Dyn2-Pac11 pep2 mixture and 1 µl of the 1-ml well solution (0.4 M sodium phosphate monobasic, 0.1 M 1,6-hexanediol, and 25% polyethylene glycol 3350). Crystals grew at 20°C into thin, individual plates over a 2-wk period. Crystals were transferred into a cryoprotectant containing well solution supplemented with 20% ethylene glycol and flash frozen in liquid nitrogen.

Data collection, structure determination, and refinement

Diffraction data were collected on a single Dyn2-Pac11 pep2 crystal at the Advanced Photon Source SER-CAT beamline 22-ID at 100 K with 1° oscillations over 180° from a single crystal. Data were indexed, integrated, and scaled in the space group $C222_1$ using HKL2000 (Otwinowski and Minor, 1997). The structure was determined using the AutoMR molecular replacement program (PHENIX crystallographic suite; Adams *et al.*, 2010) and a modified 4DS1 coordinate file (Romes *et al.*, 2012) in which a monomeric, apo Dyn2 search model was used. The model was built using AutoBuild (PHENIX; Adams *et al.*, 2010) and refined iteratively through manual builds in Coot (Emsley *et al.*, 2010) followed by refinement runs using phenix.refine (PHENIX; Adams *et al.*, 2010). Refinement statistics were monitored using a free *R*, calculated using 7.8% of the data, randomly excluded from refinement (Brünger, 1992).

Isothermal titration microcalorimetry

Pac11 pep2 was exchanged into buffer A using G-25 Sephadex Quick Spin Columns (Roche, Indianapolis, IN). Pac11 pep1 proved insoluble under all buffer conditions analyzed. WT Dyn2, Dyn2 H58K, and Dyn2 F76K/Y78E were individually exchanged into buffer A. Binding was measured by ITC at 26°C on an AutoITC200 (Microcal/GE Healthcare). Sequential injections, 19 × 2 µl, of 1.0 mM Pac11 pep2 were automatically injected into 200 µl of 50 µM WT Dyn2. The data were analyzed with the Origin (for ITC) 7.0 software package (Microcal/GE Healthcare), and the resulting isotherm was fitted to a single-site, independent-binding model. The experiment was performed in triplicate and the mean K_d and SD calculated. Mutant Dyn2–Pac11 pep2 binding experiments were performed with Pac11 pep2, Dyn2 H58K, and Dyn2 F76K/Y78E in buffer A using similar injection routines as described for WT Dyn2. Three different initial concentrations of injectant (Pac11 pep2) and cell (Dyn2 mutant construct) components were analyzed: 0.5 mM Pac11 pep2, 50 µM mutant Dyn2; 1.0 mM Pac11 pep2, 50 µM mutant Dyn2; and 3.0 mM Pac11 pep2, 0.3 mM mutant Dyn2. The 1.0 and 3.0 mM Pac11 pep2 stocks were resuspended directly in buffer A, and the 0.5 mM Pac11 pep2 stock was obtained after exchanging into buffer A to limit the background noise due to ionic interference. There was a significant heat of dilution recorded in the Pac11 pep2 control experiment, which used 3.0 mM Pac11 pep2 stock injected into 200 µl of buffer A. This component was subtracted from the raw heat, where 3.0 mM Pac11 pep2 was injected into the ITC cell containing either 0.3 mM Dyn2 H58K or 0.3 mM Dyn2 F76K/Y78E. No binding was observed across all three concentrations of Pac11 pep2 and mutant Dyn2 constructs analyzed.

Size exclusion chromatography and multiangle light scattering

WT Dyn2, Dyn2 H58K, and Dyn2 F76K/Y78E were exchanged into buffer A using 3-kDa Amicon Ultra Spin Concentrators (Millipore, Billerica, MA). Dyn2 WT was concentrated to 6.0 mg/ml, Dyn2 H58K to 10.0 mg/ml, and Dyn2 F76K/Y78E to 6.0 mg/ml. All Dyn2 constructs remained soluble during the concentration step. A 50-µl amount of each concentrated sample (Dyn2 WT, Dyn2 H58K, and Dyn2 F76K/Y78E) was individually injected onto a Superdex 200 10/300 GL size exclusion column (GE Healthcare) in buffer A supplemented with 0.2 g/l sodium azide and then passed consecutively through a Wyatt DAWN HELEOS II light scattering instrument and a Wyatt Optilab rEX refractometer (Wyatt Technology, Santa Barbara, CA). The light scattering and refractive index data were used to calculate the weight-averaged molar mass and the mass fraction in each peak using Wyatt Astra V software.

Generation of yeast deletion strains

All *S. cerevisiae* deletion strains were derived from the haploid strain VY263 (Kardon *et al.*, 2009), which has the dynein heavy chain gene (*DYN1*) tagged at its 3′ end with DNA encoding a HaloTag and the *NIP100* gene deleted (genotype, see Supplemental Table S1). *DYN1* is also fused at its 3′ end to DNA encoding an N-terminal ZZ tag for binding to immunoglobulin G (IgG) beads, a TEV cleavage site, a linker that promotes the efficiency of TEV protease, and green fluorescent protein. Gene deletion was performed via homologous recombination. Yeast transformations were performed by standard LiAc/polyethylene glycol protocol (Goldstein and McCusker, 1999). Stitched DNA fragments were amplified by standard PCR protocol. For deletion of *DYN2*, the pAG25 plasmid encoded marker nourseothricin *N*-acetyltransferase was used as template. For *PAC11* deletion, the pAG32 plasmid encoded marker hygromycin B phosphotransferase was used as template. Deletions were confirmed by DNA sequencing.

Dynein expression, purification, and TMR labeling

Dynein was purified using an established protocol (Reck-Peterson *et al.*, 2006). A 2-l yeast culture was grown to OD_{600} ~1.0 and harvested by centrifugation at 1500 × *g* for 8 min at 4°C. The pellet was washed once with double-distilled H_2O (ddH_2O) and then added dropwise into liquid nitrogen. To lyse cells, frozen droplets were ground in a coffee grinder (KitchenAid, Benton Harbor, MI) and solubilized in lysis buffer (30 mM HEPES, 50 mM potassium acetate, 2 mM magnesium acetate, 1 mM ethylene glycol tetraacetic acid [EGTA], 10% [vol/vol] glycerol, and 0.2% [vol/vol] Triton X-100, pH 7.4, supplemented with protease inhibitors, 1 mM dithiothreitol [DTT], and 100 µM MgATP). Lysate was clarified by centrifugation at 387,000 × *g* for 30 min at 4°C. Supernatant was incubated with 250 µl of IgG beads (GE Healthcare) and nutated at 4°C for 1 h. The bead slurry was poured into a column (Bio-Rad, Hercules, CA), and washed two times with 5 ml of lysis buffer. To label Dyn1, 0.5 µl of 1 mM TMR–labeled HaloTag ligand (Promega, Madison, WI) was

added, mixed well with the IgG beads, incubated at room temperature for 10 min, and washed twice with 5 ml TEV buffer (10 mM Tris-HCl, 150 mM KCl, 10% [vol/vol] glycerol, and 0.1% [vol/vol] Triton X-100, pH 7.5, 500 µM Pefabloc, 1 mM DTT, and 100 µM MgATP). IgG beads were transferred to a 2-ml Eppendorf tube, and 2.5 µl of ProTEV protease (Invitrogen, Carlsbad, CA) was added to cleave the dynein off the beads. The mixture was nutated at 16°C for 1 h and centrifuged at 20,800 × *g*, and the dynein-containing supernatant was aliquotted, flash frozen in liquid nitrogen, and stored at –80°C. Further purification to select for active Dyn1 by microtubule affinity and ATP-induced release is often performed. However, we did not do so here in order to preserve the different populations of Dyn1 complexes caused by the deletion of *Dyn2*/*Pac11* (i.e., active/inactive monomeric, dimeric and aggregated Dyn1, respectively; Figures 6 and 8).

Single-molecule dynein motility assay

To prepare coverslips for single-molecule fluorescence assays, coverslips were submerged into 25% HNO_3 for 10 min, washed twice with ddH_2O, transferred to 2 M NaOH, and incubated for 10 min. Coverslips were then washed six times with ddH_2O and air dried on a heat block. Flow chambers were generated by placing a coverslip onto a glass slide with parallel tracks of double-sided sticky tape. Taxol-stabilized MTs (Cytoskeleton, Denver, CO) were labeled with NHS-monofunctional Cy5 (GE Healthcare) following a published protocol (Peloquin *et al.*, 2005). DMB was used in all experiments unless otherwise specified (30 mM HEPES, 2 mM $MgCl_2$, 1 mM EGTA, 1 mM DTT, 10 µM Taxol, pH 7.2). To immobilize MTs on the coverslip, 10 µl of 0.2 mg/ml monomeric rigor kinesin-1 (T93N mutant; Nakata and Hirokawa, 1995) was flowed into the chamber and incubated for 2 min, followed by 20 µl of blocking solution (2 mg/ml bovine serum albumin [BSA] and 1 mg/ml β-casein) for 2 min. Twenty microliters of 0.1 mg/ml Cy5-labeled MTs (labeled tubulin:unlabeled tubulin ratio, 1:20) was flowed in the chamber and incubated for 2 min. Dynein was diluted into DMB supplemented with 2 mg/ml BSA, 2 mM Trolox, 1 mM MgATP, oxygen scavenge system (0.4% [wt/vol] glucose, 1 mg/ml glucose oxidase, and 0.04 mg/ml catalase; Shi *et al.*, 2010) and ATP regeneration system (1% pyruvate kinase and 10 mM phosphoenolpyruvate). Of this solution, 2 × 20 µl was flowed into the ~10-µl chamber, and the system was sealed with vacuum grease.

The sample was mounted on a TIRF microscope (Eclipse Ti; Nikon, Melville, NY) with a 100×/numerical aperture 1.45 oil immersion objective. The sample was excited by a 635-nm laser (Radius; Coherent, Santa Clara, CA) to visualize Cy5-labeled MTs and by a 532-nm laser (Sapphire; Coherent) to visualize TMR-labeled motors. The TMR fluorescence signal was collected for 5 min with an acquisition time of 500 ms per frame under constant illumination on an electron-multiplying charge-coupled device (EMCCD) camera (iXon Ultra; Andor, Belfast, United Kingdom) using NIS-elements imaging software (Nikon). Velocity, processivity, and the number of TMR-labeled motors from a diffraction-limited spot were analyzed using a custom Matlab, version 7.10.0 (MathWorks, Natick, MA) program described in the Supplemental Materials and Methods. The velocity for each motor was averaged over its moving distance, and long pause times were excluded from the calculation. For processivity calculation, a lower run-length cutoff of 0.5 µm was applied (the pixel size is 160 nm, and at least three pixels are necessary to distinguish a moving trace). Data were processed using Origin (OriginLab, Northampton, MA). Note that the run-length measurements are not significantly affected by the photobleaching of TMR: the characteristic time before photobleaching of TMR under our experimental conditions is 271 s (k_{bleach} = 0.0037 s^{-1}; Supplemental Figure S6), whereas the WT motor needs on average only a time of 16.5 s for its characteristic run length of 2.2 µm (v = 133 nm/s; Figure 6, B and C).

Labeling of anti-Myc antibody with Cy5

NHS-monofunctional Cy5 (GE Healthcare; 0.4 µl of 10 mg/ml) was added to 20 µl of 1 mg/ml anti-Myc antibody (ab9106, rabbit polyclonal; Abcam, Cambridge, MA) and incubated at room temperature for 30 min in the dark. The free dye molecules were removed by centrifugation: the solution was transferred to a 0.5-ml centrifugal filter unit with a 100-kDa membrane (Millipore Amicon Ultra) and washed four times with 0.5 ml of 1× phosphate-buffered saline each time by centrifugation at 20,000 × *g* for 5 min at 4°C. The labeling ratio was determined using a NanoPhotometer (Implen, Westlake Village, CA), and the labeled antibody was stored at 4°C in the dark.

Single-molecule Dyn1-Pac11 colocalization assay

The coverslip was cleaned and the flow chamber was constructed as done for the motility assays. The following steps were performed sequentially: 1) labeled antibody was diluted 10,000× in 30 mM HEPES, 2 mM $MgCl_2$, and 1 mM EGTA with 0.5 mg/ml BSA (pH 7.2), and 20 µl of diluted solution was flowed into the chamber and incubated for 2 min; 2) 20 µl of blocking buffer (BB; 30 mM HEPES, 2 mM $MgCl_2$, 1 mM EGTA, with 5 mg/ml BSA and 1 mg/ml β-casein, pH 7.2) was flowed into the chamber and incubated for 5 min; 3) 20 µl of diluted motors (the same dilution used for the motility assays) in BB was added and incubated for 5 min; 4) 20 µl of diluted antibody solution was flowed into the chamber and incubated for 5 min; 5) the chamber was then washed twice with 20 µl of BB containing an oxygen scavenger system and 2 mM Trolox; and 6) the chamber was sealed with vacuum grease. The acquisition parameters were the same as for the motility assays, except that 10 frames were collected instead of 600. The images shown in Figure 7B and Supplemental Figure S4 are the averages of the 10 image frames acquired for each experiment.

This approach resulted in sparse nonspecific binding to the glass surface by antibodies, Dyn1, Pac11-Dyn1, and Pac11, in addition to specific binding of Pac11 and Pac11-Dyn1 to the surface-bound antibodies. The second round of antibody incubation ensured recognition of Pac11 on nonspecifically bound complexes as well (e.g., on Dyn1-Pac11 complexes bound to the glass via Dyn1), although some Dyn1-Pac11 complexes could have bound the surface in a manner that prevented antibody access. Although an initial increase of the incubation time of 2–5 min for the second round of antibody incubation led to an increased binding of anti-Myc antibody to Dyn1-associated Pac11 (resulting in an increased Cy5-TMR colocalization for Dyn1 purified from the WT strain), we refrained from increasing the incubation time further due to an increased background signal resulting from the nonspecific binding of the Cy5-labeled antibody to the coverslip surface. Thus, the degree of Pac11-Dyn1 colocalization obtained from this method represents a lower boundary, and the actual degree of Pac11-Dyn1 colocalization could be significantly greater.

For all three strains, the binding of Dyn1 to the coverslip was similar. However whereas ~60% of TMR-labeled Dyn1 colocalized with the Cy5-labeled anti-Myc antibody in the WT (implying complex formation of 60% or more of Dyn1 and Pac11 proteins), no colocalization was observed in either of the deletion strains. This simultaneously demonstrates that the antibody does not cross-react with Dyn1 and that in the absence of Dyn2, Pac11 fails to bind to Dyn1.

Western blot analysis

The protein concentrations of TEV-released Dyn1 purified from WT, *dyn2*Δ, and *dyn2*Δ*pac11*Δ strains were determined by SDS–PAGE analysis using Krypton stain (Pierce, Rockford, IL) and BSA protein concentration standards. Western blot analysis was conducted on the TEV-released motor fraction from each strain after loading amounts of Dyn1 that had been normalized across strains. Pac11 and Dyn2 were detected using rabbit anti-Myc antibody (1:2000; Abcam) and rabbit anti-Dyn2 antibody (1:200; Stelter *et al.*, 2007), respectively, and an Alexa Fluor 680–labeled anti-rabbit secondary antibody (1:5000; Life Technologies, Carlsbad, CA).

Coordinate deposition

Atomic coordinates and structure factors for the Dyn2-Pac11 pep2 complex have been deposited in the Protein Data Bank, Research Collaboratory for Structural Bioinformatics, Rutgers University, New Brunswick, NJ (www.rcsb.org/) under accession code 4HT6.

ACKNOWLEDGMENTS

We thank Ed Hurt for generously providing the anti-Dyn2 antibody and Ciyu Yang and Marion Schmidt for stimulating discussions about the generation of *S. cerevisiae* deletion strains and providing pAG25 and pAG32 plasmids. This work was supported by National Institutes of Health Grants R01GM094415 (to K.C.S.) and R01GM098469 (to A.G.) and March of Dimes Grant FY11-434 (to K.C.S.). M.P.N. received support from the National Institutes of Health–funded Medical Scientist Training Program T32 GM007288 at the Albert Einstein College of Medicine, and S.B. received support from German Research Foundation Grant BR 4257/1-1 as well as National Institutes of Health Grant R01GM098469; the latter also supported L.R. The University of North Carolina Program in Molecular and Cellular Biophysics is supported under National Institutes of Health T32GM008570.

REFERENCES

Adames NR, Cooper JA (2000). Microtubule interactions with the cell cortex causing nuclear movements in *Saccharomyces cerevisiae*. J Cell Biol 149, 863–874.

Adams PD *et al.* (2010). PHENIX: a comprehensive Python-based system for macromolecular structure solution. Acta Crystallogr D Biol Crystallogr 66, 213–221.

Bader JR, Vaughan KT (2010). Dynein at the kinetochore: timing, interactions and functions. Semin Cell Dev Biol 21, 269–275.

Benison G, Karplus PA, Barbar E (2008). The interplay of ligand binding and quaternary structure in the diverse interactions of dynein light chain LC8. J Mol Biol 384, 954–966.

Brünger AT (1992). Free *R* value: a novel statistical quantity for assessing the accuracy of crystal structures. Nature 355, 472–475.

Burgess SA, Walker ML, Sakakibara H, Knight PJ, Oiwa K (2003). Dynein structure and power stroke. Nature 421, 715–718.

Carter AP, Cho C, Jin L, Vale RD (2011). Crystal structure of the dynein motor domain. Science 331, 1159–1165.

Carter AP, Garbarino JE, Wilson-Kubalek EM, Shipley WE, Cho C, Milligan RA, Vale RD, Gibbons IR (2008). Structure and functional role of dynein's microtubule-binding domain. Science 322, 1691–1695.

Deng W, Garrett C, Dombert B, Soura V, Banks G, Fisher EM, van der Brug MP, Hafezparast M (2010). Neurodegenerative mutation in cytoplasmic dynein alters its organization and dynein-dynactin and dynein-kinesin interactions. J Biol Chem 285, 39922–39934.

Emsley P, Lohkamp B, Scott WG, Cowtan K (2010). Features and development of Coot. Acta Crystallogr D Biol Crystallogr 66, 486–501.

Eshel D, Urrestarazu LA, Vissers S, Jauniaux JC, van Vliet-Reedijk JC, Planta RJ, Gibbons IR (1993). Cytoplasmic dynein is required for normal nuclear segregation in yeast. Proc Natl Acad Sci USA 90, 11172–11176.

Farkasovsky M, Küntzel H (2001). Cortical Num1p interacts with the dynein intermediate chain Pac11p and cytoplasmic microtubules in budding yeast. J Cell Biol 152, 251–262.

Geiser JR, Schott EJ, Kingsbury TJ, Cole NB, Totis LJ, Bhattacharyya G, He L, Hoyt MA (1997). *Saccharomyces cerevisiae* genes required in the absence of the CIN8-encoded spindle motor act in functionally diverse mitotic pathways. Mol Biol Cell 8, 1035–1050.

Gennerich A, Carter AP, Reck-Peterson SL, Vale RD (2007). Force-induced bidirectional stepping of cytoplasmic dynein. Cell 131, 952–965.

Gill SR, Cleveland DW, Schroer TA (1994). Characterization of DLC-A and DLC-B, two families of cytoplasmic dynein light chain subunits. Mol Biol Cell 5, 645–654.

Goldstein AL, McCusker JH (1999). Three new dominant drug resistance cassettes for gene disruption in *Saccharomyces cerevisiae*. Yeast 15, 1541–1553.

Hafezparast M *et al.* (2003). Mutations in dynein link motor neuron degeneration to defects in retrograde transport. Science 300, 808–812.

Hall J, Song Y, Karplus PA, Barbar E (2010). The crystal structure of dynein intermediate chain-light chain roadblock complex gives new insights into dynein assembly. J Biol Chem 285, 22566–22575.

Ho Y *et al.* (2002). Systematic identification of protein complexes in *Saccharomyces cerevisiae* by mass spectrometry. Nature 415, 180–183.

Hódi Z, Nemeth AL, Radnai L, Hetenyi C, Schlett K, Bodor A, Perczel A, Nyitray L (2006). Alternatively spliced exon B of myosin Va is essential for binding the tail-associated light chain shared by dynein. Biochemistry 45, 12582–12595.

Hrabé de Angelis MH *et al.* (2000). Genome-wide, large-scale production of mutant mice by ENU mutagenesis. Nat Genet 25, 444–447.

Imamula K, Kon T, Ohkura R, Sutoh K (2007). The coordination of cyclic microtubule association/dissociation and tail swing of cytoplasmic dynein. Proc Natl Acad Sci USA 104, 16134–16139.

Kardon JR, Reck-Peterson SL, Vale RD (2009). Regulation of the processivity and intracellular localization of *Saccharomyces cerevisiae* dynein by dynactin. Proc Natl Acad Sci USA 106, 5669–5674.

Karki S, Holzbaur EL (1995). Affinity chromatography demonstrates a direct binding between cytoplasmic dynein and the dynactin complex. J Biol Chem 270, 28806–28811.

King SJ, Bonilla M, Rodgers ME, Schroer TA (2002). Subunit organization in cytoplasmic dynein subcomplexes. Protein Sci 11, 1239–1250.

King SJ, Brown CL, Maier KC, Quintyne NJ, Schroer TA (2003). Analysis of the dynein-dynactin interaction in vitro and in vivo. Mol Biol Cell 14, 5089–5097.

Kini AR, Collins CA (2001). Modulation of cytoplasmic dynein ATPase activity by the accessory subunits. Cell Motil Cytoskeleton 48, 52–60.

Kon T, Mogami T, Ohkura R, Nishiura M, Sutoh K (2005). ATP hydrolysis cycle-dependent tail motions in cytoplasmic dynein. Nat Struct Mol Biol 12, 513–519.

Kon T, Nishiura M, Ohkura R, Toyoshima YY, Sutoh K (2004). Distinct functions of nucleotide-binding/hydrolysis sites in the four AAA modules of cytoplasmic dynein. Biochemistry 43, 11266–11274.

Kon T, Oyama T, Shimo-Kon R, Imamula K, Shima T, Sutoh K, Kurisu G (2012). The 2.8 A crystal structure of the dynein motor domain. Nature 484, 345–350.

Lee WL, Kaiser MA, Cooper JA (2005). The offloading model for dynein function: differential function of motor subunits. J Cell Biol 168, 201–207.

Lee WL, Oberle JR, Cooper JA (2003). The role of the lissencephaly protein Pac1 during nuclear migration in budding yeast. J Cell Biol 160, 355–364.

Li J, Lee WL, Cooper JA (2005). NudEL targets dynein to microtubule ends through LIS1. Nat Cell Biol 7, 686–690.

Li YY, Yeh E, Bloom K (1993). Disruption of mitotic spindle orientation in a yeast dynein mutant. Proc Natl Acad Sci USA 90, 10096–10100.

Liang J, Jaffrey SR, Guo W, Snyder SH, Clardy J (1999). Structure of the PIN/LC8 dimer with a bound peptide. Nat Struct Biol 6, 735–740.

Makokha M, Hare M, Li M, Hays T, Barbar E (2002). Interactions of cytoplasmic dynein light chains Tctex-1 and LC8 with the intermediate chain IC74. Biochemistry 41, 4302–4311.

Mok YK, Lo KW, Zhang M (2001). Structure of Tctex-1 and its interaction with cytoplasmic dynein intermediate chain. J Biol Chem 276, 14067–14074.

Moore JK, Li J, Cooper JA (2008). Dynactin function in mitotic spindle positioning. Traffic 9, 510–527.

Nakata T, Hirokawa N (1995). Point mutation of adenosine triphosphate-binding motif generated rigor kinesin that selectively blocks anterograde lysosome membrane transport. J Cell Biol 131, 1039–1053.

Numata N, Shima T, Ohkura R, Kon T, Sutoh K (2011). C-sequence of the *Dictyostelium* cytoplasmic dynein participates in processivity modulation. FEBS Lett 585, 1185–1190.

Nyarko A, Cochrun L, Norwood S, Pursifull N, Voth A, Barbar E (2005). Ionization of His 55 at the dimer interface of dynein light-chain LC8 is coupled to dimer dissociation. Biochemistry 44, 14248–14255.
Nyarko A, Hall J, Hall A, Hare M, Kremerskothen J, Barbar E (2011). Conformational dynamics promote binding diversity of dynein light chain LC8. Biophys Chem 159, 41–47.
Ori-McKenney KM, Xu J, Gross SP, Vallee RB (2010). A cytoplasmic dynein tail mutation impairs motor processivity. Nat Cell Biol 12, 1228–1234.
Otwinowski Z, Minor W (1997). Processing of x-ray diffraction data collected in oscillation mode. Methods Enzymol 276, 307–326.
Peloquin J, Komarova Y, Borisy G (2005). Conjugation of fluorophores to tubulin. Nat Methods 2, 299–303.
Pfarr CM, Coue M, Grissom PM, Hays TS, Porter ME, McIntosh JR (1990). Cytoplasmic dynein is localized to kinetochores during mitosis. Nature 345, 263–265.
Qiu R, Zhang J, Xiang X (2013). Identification of a novel site in the tail of dynein heavy chain important for dynein function in vivo. J Biol Chem 288, 2271–2280.
Radnai L *et al*. (2010). Affinity, avidity, and kinetics of target sequence binding to LC8 dynein light chain isoforms. J Biol Chem 285, 38649–38657.
Rapali P, Szenes A, Radnai L, Bakos A, Pal G, Nyitray L (2011). DYNLL/LC8: a light chain subunit of the dynein motor complex and beyond. FEBS J 278, 2980–2996.
Reck-Peterson SL, Yildiz A, Carter AP, Gennerich A, Zhang N, Vale RD (2006). Single-molecule analysis of dynein processivity and stepping behavior. Cell 126, 335–348.
Roberts AJ *et al*. (2009). AAA+ Ring and linker swing mechanism in the dynein motor. Cell 136, 485–495.
Romes EM, Tripathy A, Slep KC (2012). Structure of a yeast Dyn2-Nup159 complex and molecular basis for dynein light chain-nuclear pore interaction. J Biol Chem 287, 15862–15873.
Ross JL, Wallace K, Shuman H, Goldman YE, Holzbaur EL (2006). Processive bidirectional motion of dynein-dynactin complexes in vitro. Nat Cell Biol 8, 562–570.
Saunders WS, Koshland D, Eshel D, Gibbons IR, Hoyt MA (1995). *Saccharomyces cerevisiae* kinesin- and dynein-related proteins required for anaphase chromosome segregation. J Cell Biol 128, 617–624.
Schmidt H, Gleave ES, Carter AP (2012). Insights into dynein motor domain function from a 3.3-A crystal structure. Nat Struct Mol Biol 19, 492–497, S491.
Shi X, Lim J, Ha T (2010). Acidification of the oxygen scavenging system in single-molecule fluorescence studies: in situ sensing with a ratiometric dual-emission probe. Anal Chem 82, 6132–6138.
Signor D, Wedaman KP, Orozco JT, Dwyer ND, Bargmann CI, Rose LS, Scholey JM (1999). Role of a class DHC1b dynein in retrograde transport of IFT motors and IFT raft particles along cilia, but not dendrites, in chemosensory neurons of living *Caenorhabditis elegans*. J Cell Biol 147, 519–530.
Sivagurunathan S, Schnittker RR, Nandini S, Plamann MD, King SJ (2012). A mouse neurodegenerative dynein heavy chain mutation alters dynein motility and localization in *Neurospora crassa*. Cytoskeleton (Hoboken) 69, 613–624.
Stelter P, Kunze R, Flemming D, Hopfner D, Diepholz M, Philippsen P, Bottcher B, Hurt E (2007). Molecular basis for the functional interaction of dynein light chain with the nuclear-pore complex. Nat Cell Biol 9, 788–796.
Steuer ER, Wordeman L, Schroer TA, Sheetz MP (1990). Localization of cytoplasmic dynein to mitotic spindles and kinetochores. Nature 345, 266–268.
Stuchell-Brereton MD, Siglin A, Li J, Moore JK, Ahmed S, Williams JC, Cooper JA (2011). Functional interaction between dynein light chain and intermediate chain is required for mitotic spindle positioning. Mol Biol Cell 22, 2690–2701.
Susalka SJ, Nikulina K, Salata MW, Vaughan PS, King SM, Vaughan KT, Pfister KK (2002). The roadblock light chain binds a novel region of the cytoplasmic dynein intermediate chain. J Biol Chem 277, 32939–32946.
Tang X, Germain BS, Lee WL (2012). A novel patch assembly domain in Num1 mediates dynein anchoring at the cortex during spindle positioning. J Cell Biol 196, 743–756.
Trokter M, Mücke N, Surrey T (2012). Reconstitution of the human cytoplasmic dynein complex. Proc Natl Acad Sci USA 109, 20895–20900.
Tulu US, Fagerstrom C, Ferenz NP, Wadsworth P (2006). Molecular requirements for kinetochore-associated microtubule formation in mammalian cells. Curr Biol 16, 536–541.
Tynan SH, Gee MA, Vallee RB (2000). Distinct but overlapping sites within the cytoplasmic dynein heavy chain for dimerization and for intermediate chain and light intermediate chain binding. J Biol Chem 275, 32769–32774.
Vale RD (2003). The molecular motor toolbox for intracellular transport. Cell 112, 467–480.
Wagner W, Fodor E, Ginsburg A, Hammer JA 3rd (2006). The binding of DYNLL2 to myosin Va requires alternatively spliced exon B and stabilizes a portion of the myosin's coiled-coil domain. Biochemistry 45, 11564–11577.
Wickstead B, Gull K (2007). Dyneins across eukaryotes: a comparative genomic analysis. Traffic 8, 1708–1721.
Williams JC, Roulhac PL, Roy AG, Vallee RB, Fitzgerald MC, Hendrickson WA (2007). Structural and thermodynamic characterization of a cytoplasmic dynein light chain-intermediate chain complex. Proc Natl Acad Sci USA 104, 10028–10033.
Williams JC, Xie H, Hendrickson WA (2005). Crystal structure of dynein light chain TcTex-1. J Biol Chem 280, 21981–21986.

SUPPLEMENTAL MATERIAL

SUPPLEMENTAL MATERIALS AND METHODS

Kymograph analysis

In contrast to nanometer-scale tracking of bright fluorescent molecules using 2D Gaussian fitting algorithms, kymographs offer a quick and easy way to extract information about motor velocity and processivity without needing to localize dye molecules with sub-pixel precision. Generally, kymographs of fluorescence-tagged microtubule (MT) motors are made using a single, hand-drawn path along the MT long axis. For each image in the acquired time series, the intensity profile is calculated along this path, with each profile composing a single column of pixels along the spatial axis of the output image. Repeating this process for all frames yields the equivalent of a graph that plots the motor trajectory, i.e. position vs. time or as commonly done, time vs. position (Fig. 6A, main text).

Unfortunately, in practice, it is tedious and difficult to draw a single-pixel path such that the maximum intensity of every fluorescent spot always falls along the selected pixels (e.g. due to fluctuations in motor position along the direction orthogonal to the MT, long-term stage drift, small imprecisions in drawing of the line, etc.). As a result, even if the fluorescence intensity were absolutely constant, the intensity of the path traced-out in the kymograph can vary considerably, giving the false impression that the dye intensity fluctuates in time (in reality, the fluorescence intensity does fluctuate, due to the inherent photophysics, and the artificial fluctuations are added to this behavior). In other words, because the kymograph does not integrate the spot intensity over space, but rather shows a single line profile through an arbitrary point on the spot, information about the spot brightness is discarded, and artificial noise is introduced. This degrades the quality of the kymograph image, and also precludes quantitative analysis of the path intensities.

We solved this problem by creating a composite kymograph from several individual kymographs that are derived from paths parallel to the original one. First, as in a traditional kymograph, a path is drawn along the MT axis, and a kymograph is constructed from this line and saved. Next, the path is displaced by ±0.5 pixels perpendicular to the original path (so the paths are all parallel) and kymographs are again created from these paths and saved (intensities are calculated using the MATLAB 'improfile()' function, which interpolates inter-pixel values along line segments). The process is repeated four times, yielding a total of nine kymographs. While the intensities of the motor trajectories traced out in each of these kymographs varies, the trajectories themselves essentially overlap. These images are averaged together to create the final composite kymograph. This strategy makes use of the fact that the intensity missed by any individual kymograph will be detected by others derived from the parallel paths (i.e. it is an approximate integration over the intensity of the fluorescent spots). Consequently, variations in intensity of the paths in the composite kymograph are attributable to true variations in emitted fluorescence. This allows us to reliably quantify the number of fluorophores attached to each moving particle.

To analyze the fluorescence intensities using the improved kymograph, we identify the maximum intensity for each trajectory at each point in time. The trajectories are identified manually by drawing a path through the approximate center of each one. For each point in time, i.e. column of pixels in the kymograph, a search is conducted in 0.5 pixel increments above and below the point marked by the manually drawn path, and the maximum value is recorded. This technique precludes erroneous measurement of intensity fluctuations that would otherwise arise due to variations in motor velocity on short time scales, if only the approximate, manually drawn path were considered. For each path, plotting a histogram of intensities allows rapid, precise comparison of intensities between different particles (by comparing mean intensities), and determination of photobleaching over time (multi-modal distributions).

The methods described above allow rapid determination of motor velocity, run length, and stoichiometry without the computational demands of single-particle tracking. We have written user-friendly software to help perform this analysis, which we will describe in detail in a future publication.

SUPPLEMENTAL FIGURES

FIGURE S1. Hydrogen-bonding network matrix comparing the interactions between Dyn2 and Pac11 pep2 (upper horizontal axis) determined in this study with the previously reported interactions between Dyn2 and Nup159 pep2 (lower horizontal axis)(Romes *et al.*, 2012). Secondary structure is indicated along the axes as are residues involved in the interactions and their respective chain label. The top half of a grid square represents hydrogen bonds between Dyn2 and Pac11 pep2 while the bottom half represents hydrogen bonds between Dyn2 and Nup159 pep2. Backbone/backbone, side chain/side chain and backbone/side chain hydrogen bonds are colored blue, green, and red respectively. The number of hydrogen bonds that occur between two residues is one unless otherwise noted in by a "2" in the cell, indicative of two hydrogen bonds occurring between these residues. Where two of the designated hydrogen bonding classes occur between residues, the cell is split diagonally with each half colored accordingly.

FIGURE S2. Dyn2 is a homodimer in solution. SEC-MALS of WT Dyn2 was performed by injecting 50 µL of 6 mg/mL Dyn2 at pH 6.8. The differential refractive index was normalized to the dimer peak (21.6 kDa) and is shown in grey. Peaks from the differential refractive index display the measured molecular weight (black trace) with the corresponding fraction of total injected mass in parentheses. The WT Dyn2 construct has a calculated molecular weight of 10.9 kDa.

FIGURE S3. Dyn2 mutations at the Pac11 pep2 binding site as well as the Dyn2 homodimerization interface abrogate the ability of Dyn2 to bind Pac11 pep2 as detected using ITC. **A**. The upper panel shows heat generated by 19 x 2 µL sequential injections of 0.5 mM Pac11 pep2 (desalted using a G-25 Sephadex column, see Materials and Methods section), injected into the ITC cell containing 200 µL of 50 µM Dyn2 F76K/Y78E. The bottom panel shows normalized heat (Kcal/Mole of injectant) versus the molar ratio of Pac11 pep2:Dyn2 F76K/Y78E. No binding was detected. **B**. A control experiment in which an elevated concentration of Pac11 pep2 (3mM) obtained without desalting, was injected into the ITC cell containing 200 µL of sample buffer using the same injection protocol as in A. Exothermic heat of dilution was detected. **C**. Same as in B except the ITC cell contained 200 µL of 0.3 mM Dyn2 F76K/Y78E. The bottom panel shows normalized heat (Kcal/Mole of injectant) versus the molar ratio of Pac11 pep2:Dyn2 F76K/Y78E after subtracting the heat of dilution of Pac11 pep2 obtained in B. No binding was detected. **D**. Same as in A except the injectant was 0.5 mM Pac11 pep2 (desalted) and the ITC cell contained 200 µL of 50 µM Dyn2 H58K. No binding was detected. **E**. Same as in A except the injectant was 3 mM Pac11 pep2 (not desalted), and the ITC cell contained 200 µL of 0.3 mM Dyn2 H58K. No binding was detected.

FIGURE S4. TIRF-based, single-molecule fluorescence analysis confirms that the majority of TMR-labeled Dyn1 molecules purified from the WT strain is bound to Pac11-Myc, as revealed by the ~60% co-localization (yellow) of TMR-labeled Dyn1 (red) and Cy5-labeled anti-Myc antibodies (green) (top). In contrast, Dyn1 motors purified from the *dyn2*Δ (center) and *dyn2*Δ*pac11*Δ strains (bottom) do not show significant TMR-Cy5

co-localization (see supplemental material for details underlying this analysis). Images represent 330 × 330 pixel subregions of the original 512 × 512 pixel EMCCD images.

FIGURE S5. The absence of Dyn2/Pac11 results in an increased number of fluorescent spots bound to the coverslip surface that contain more than two dyes, suggesting Dyn1 aggregation. **A.-C.** Images show Cy5-labeled microtubules (green) and TMR-labeled Dyn1 (red) purified from WT (A), *dyn2*Δ (B) and *dyn2*Δ*pac11*Δ (C) strains, respectively (see Materials and Methods for details) (images represent 130 × 130 pixel subregions of the original 512 × 512 pixel EMCCD images). White arrows in B and C show examples of bright fluorescent spots containing more than two dyes. The white square in B indicates the subregion shown in D. **D.** A putative dynein aggregate containing more than three dyes, as revealed by intensity analysis (F). **E.** Kymograph generated by stacking line scans along the dashed line indicated in subfigure D (averaged with two parallel scans on each side, each separated by 0.5 pixels (effective pixel size: 160 nm); note that the smaller spot to the upper left of the aggregate marked "2." is a separate spot, not included in the line scans or other analysis). The kymograph shows the binding of two different-sized dynein complexes (steps 1. and 2.), followed by the bleaching/dissociation of one of the dyes/labeled Dyn1 HC attached to the first complex. The time marked t_1 corresponds to the image shown in B. **F.** Intensity analysis of the kymograph reveals that the first complex contains two dyes initially ($2 \times \Delta I \simeq 1.3$ a.u.), while the second complex contains more than four ($>4 \times \Delta I$). After the bleaching of one TMR molecule, the remaining fluorescence of the first complex reflects the intensity of a single dye ($\Delta I \simeq 1.3$ a.u. above background).

FIGURE S6. Fluorescence time traces and photobleaching analysis of TMR-tagged Dyn1. **A.** Example traces of fluorescence signals showing i) binding of a Dyn1 molecule to the coverslip surface, followed by the stepwise bleaching of both dyes (red), ii) 1-step bleaching of a single dye (green) of a Dyn1 molecule bound to the coverslip (dimer or monomer), and iii) the surface binding of a Dyn1 molecule with one dye (blue) (see Material and Methods for details). Intensities at each time point correspond to the average intensities in a square of 5x5 pixels with the pixel registering the highest relative counts centered on the 5 x 5 grid as calculated by ImageJ (NIH) (note that the intensity values calculated here cannot be directly compared to the intensities values presented in the kymograph-based analysis, which were calculated in a different way, see Supplemental Materials and Methods, Kymograph analysis). **B.** Photobleaching of TMR-tagged Dyn1 molecules covalently bound to a BSA-coated coverslip acquired under the same biochemical (dynein motility buffer plus additives, see Materials and Methods) and photophysical conditions (fluorescence excitation intensity) as used for the single-molecule assay except that images were captured once per second. Intensities at each time point correspond to the total intensities in each acquired image. Fitting a first-order exponential decay function yields a characteristic time before bleaching of 271 ± 2 s, which corresponds to an average photobleaching rate of 0.0037 s^{-1}.

SUPPLEMENTAL REFERENCES

Kardon, J.R., Reck-Peterson, S.L., and Vale, R.D. (2009). Regulation of the processivity and intracellular localization of Saccharomyces cerevisiae dynein by dynactin. Proc Natl Acad Sci U S A *106*, 5669-5674.

Romes, E.M., Tripathy, A., and Slep, K.C. (2012). Structure of a yeast Dyn2-Nup159 complex and molecular basis for dynein light chain-nuclear pore interaction. J Biol Chem *287*, 15862-15873.

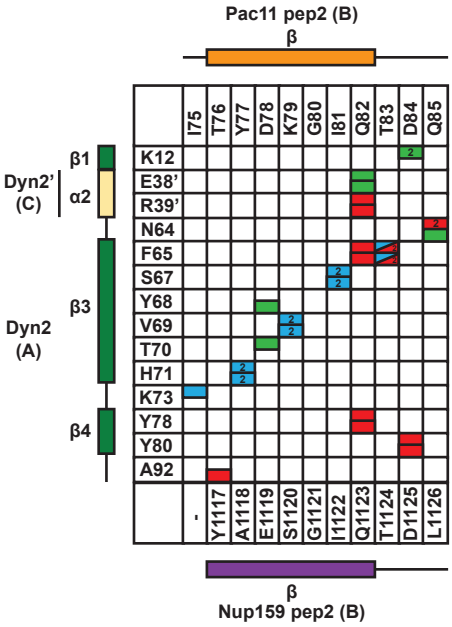
Pac11 pep2 (B)
β
I75
T76
Y77
D78
K79
G80
I81
Q82
T83
D84
Q85
β1
Dyn2'
(C)
α2
K12
E38'
R39'
N64
F65
S67
β3
Dyn2
(A)
Y68
V69
T70
H71
K73
β4
Y78
Y80
A92
-
Y1117
A1118
E1119
S1120
G1121
I1122
Q1123
T1124
D1125
L1126
β
Nup159 pep2 (B)

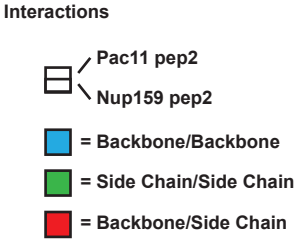
Interactions
Pac11 pep2
Nup159 pep2
= Backbone/Backbone
= Side Chain/Side Chain
= Backbone/Side Chain

Fig. S1

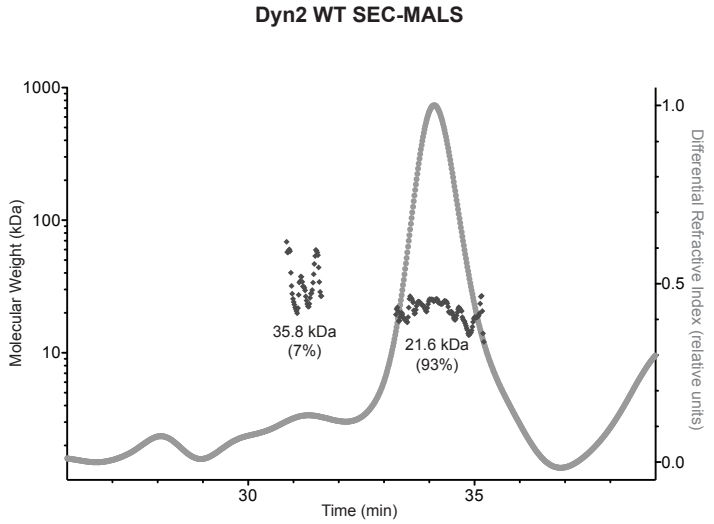
Dyn2 WT SEC-MALS
1000
100
10
Molecular Weight (kDa)
1.0
0.5
0.0
Differential Refractive Index (relative units)
35.8 kDa
(7%)
21.6 kDa
(93%)
30
35
Time (min)

Fig. S2

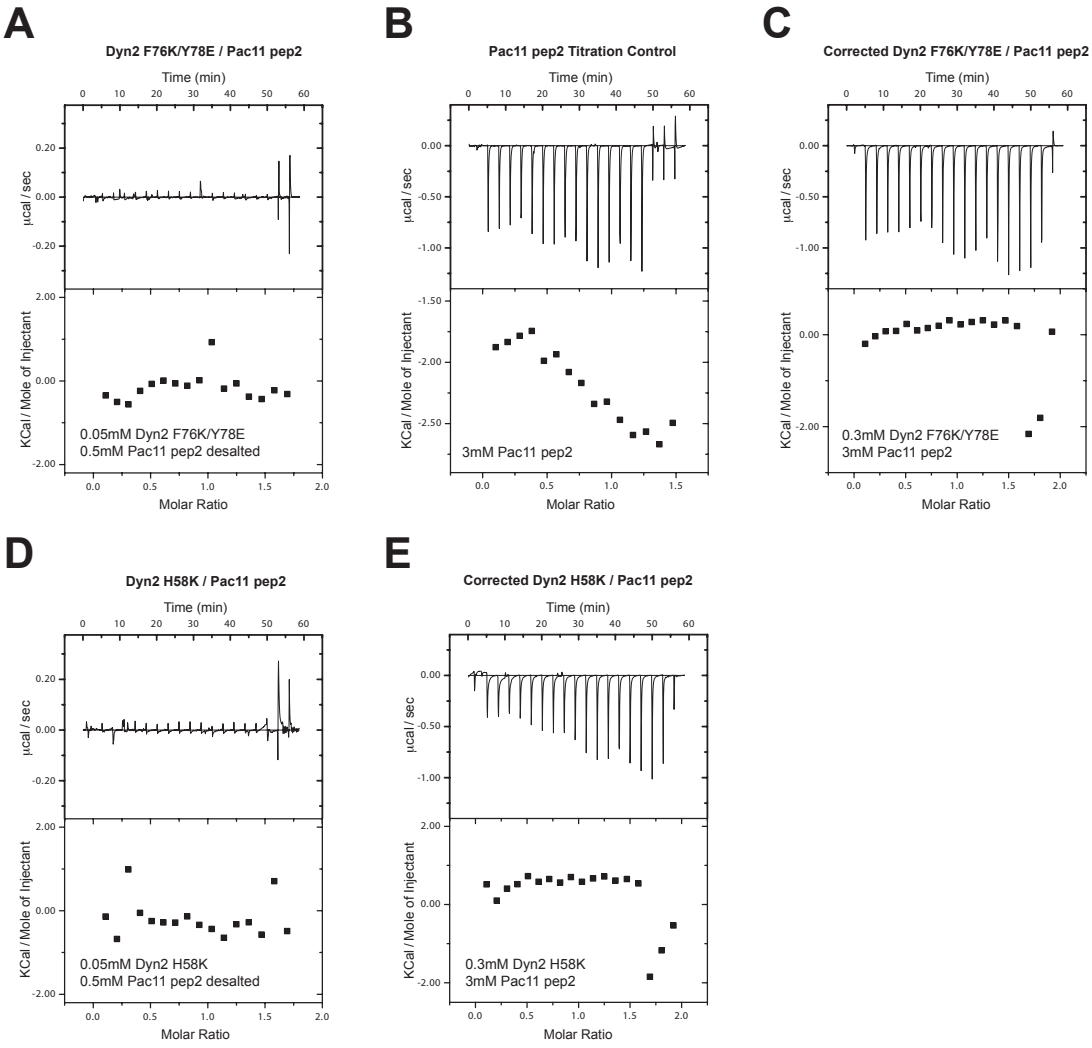
A
Dyn2 F76K/Y78E / Pac11 pep2
Time (min)
µcal / sec
KCal / Mole of Injectant
0.05mM Dyn2 F76K/Y78E
0.5mM Pac11 pep2 desalted
Molar Ratio
B
Pac11 pep2 Titration Control
Time (min)
µcal / sec
KCal / Mole of Injectant
3mM Pac11 pep2
Molar Ratio
C
Corrected Dyn2 F76K/Y78E / Pac11 pep2
Time (min)
µcal / sec
KCal / Mole of Injectant
0.3mM Dyn2 F76K/Y78E
3mM Pac11 pep2
Molar Ratio
D
Dyn2 H58K / Pac11 pep2
Time (min)
µcal / sec
KCal / Mole of Injectant
0.05mM Dyn2 H58K
0.5mM Pac11 pep2 desalted
Molar Ratio
E
Corrected Dyn2 H58K / Pac11 pep2
Time (min)
µcal / sec
KCal / Mole of Injectant
0.3mM Dyn2 H58K
3mM Pac11 pep2
Molar Ratio

Fig. S3

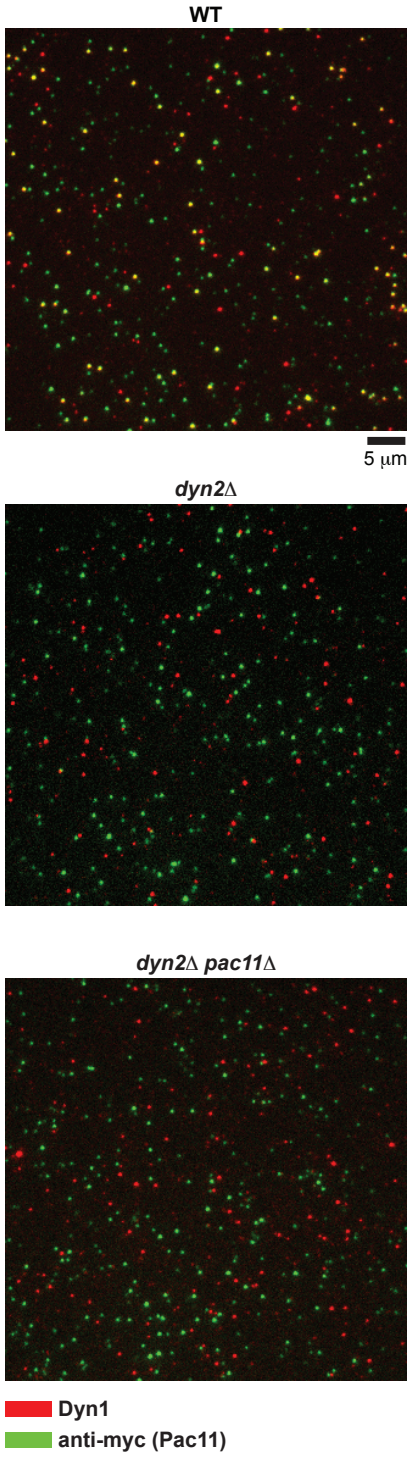

Fig. S4

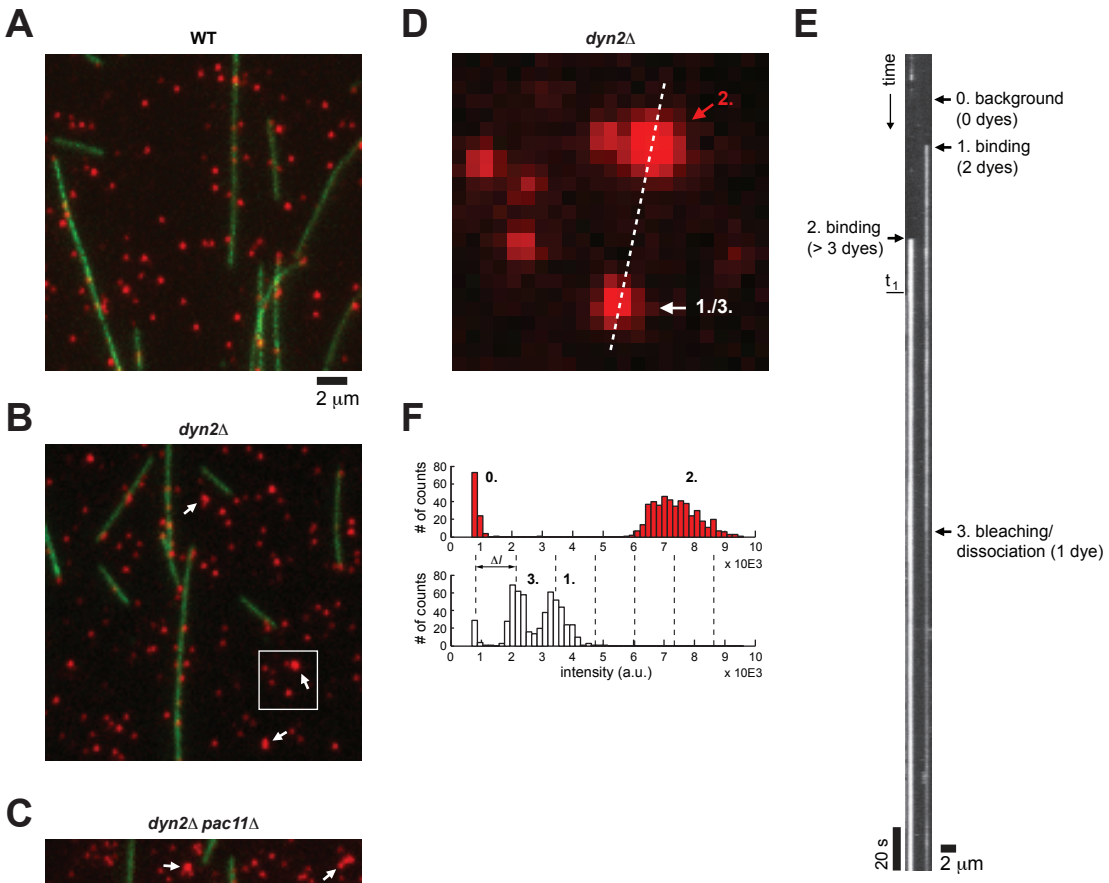
A
WT
2 μm
B
dyn2Δ
C
dyn2Δ pac11Δ
D
dyn2Δ
2.
1./3.
E
time
0. background
(0 dyes)
1. binding
(2 dyes)
2. binding
(> 3 dyes)
t1
3. bleaching/
dissociation (1 dye)
20 s
2 μm
F
# of counts
0.
2.
x 10E3
Δl
3.
1.
intensity (a.u.)

Fig. S5

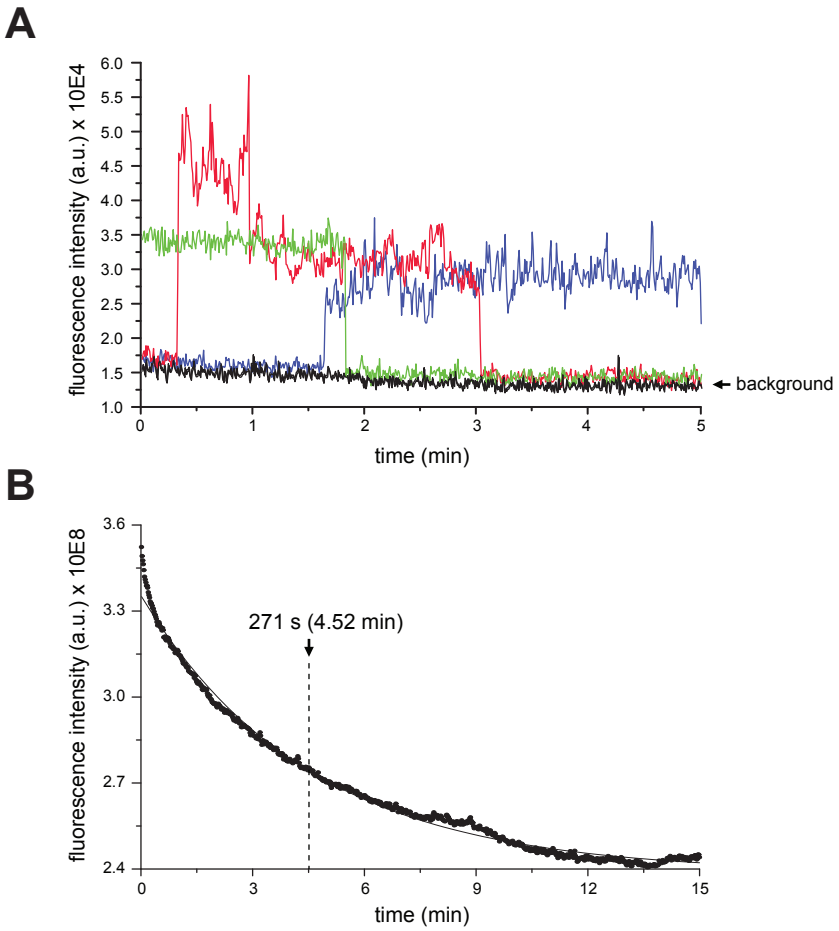
A
fluorescence intensity (a.u.) x 10E4
6.0
5.5
5.0
4.5
4.0
3.5
3.0
2.5
2.0
1.5
1.0
0
1
2
3
4
5
time (min)
background
B
fluorescence intensity (a.u.) x 10E8
3.6
3.3
3.0
2.7
2.4
271 s (4.52 min)
0
3
6
9
12
15
time (min)

Fig. S6

TABLE S1: Yeast strain genotype.

Strain	Note	Genotype	Source
VY263		pep4::HIS3, prb1Δ, PAC11-13×Myc::TRP, ZZ-TEV-GFP-3×HA-DYN1-GS-HALOTAG::KAN, nip100Δ::URA3	Kardon *et al.*, 2009.
GY4	VY263 with *dyn2Δ*	pep4::HIS3, prb1Δ, PAC11-13×Myc::TRP, ZZ-TEV-GFP-3×HA-DYN1-GS-HALOTAG::KAN, nip100Δ::URA3, dyn2Δ::NAT	this study
GY6	VY263 with *dyn2Δ* and *pac11Δ*	pep4::HIS3, prb1Δ, ZZ-TEV-GFP-3×HA-DYN1-GS-HALOTAG::KAN, nip100Δ::URA3, dyn2Δ::NAT, pac11Δ::HYG	this study

TABLE S2: Quantification of dye-labels in mobile versus immobile Dyn1 populations.

Strain	Mobile	1 dye mobile	2 dye mobile	≥3 dye mobile	1 dye immobile	2 dye immobile	≥3 dye immobile
VY263 % (n)	60.5±2.2 (885)	34.3±2.8 (535)	64.4±2.9 (535)	1.3 (535)	57.7±4.0 (350)	38.7±3.8 (350)	3.6 (350)
GY4 % (n)	21.5±1.4 (867)	30.6±4.1 (186)	68.3±4.2 (186)	1.1 (186)	81.1±1.8 (681)	17.5±1.8 (681)	1.4 (681)
GY6 % (n)	22.3±1.4 (1238)	38.1±3.9 (276)	61.6±4.0 (276)	0.3 (276)	79.9±1.8 (962)	18.5±1.7 (962)	1.6 (962)